

ORIGINAL RESEARCH

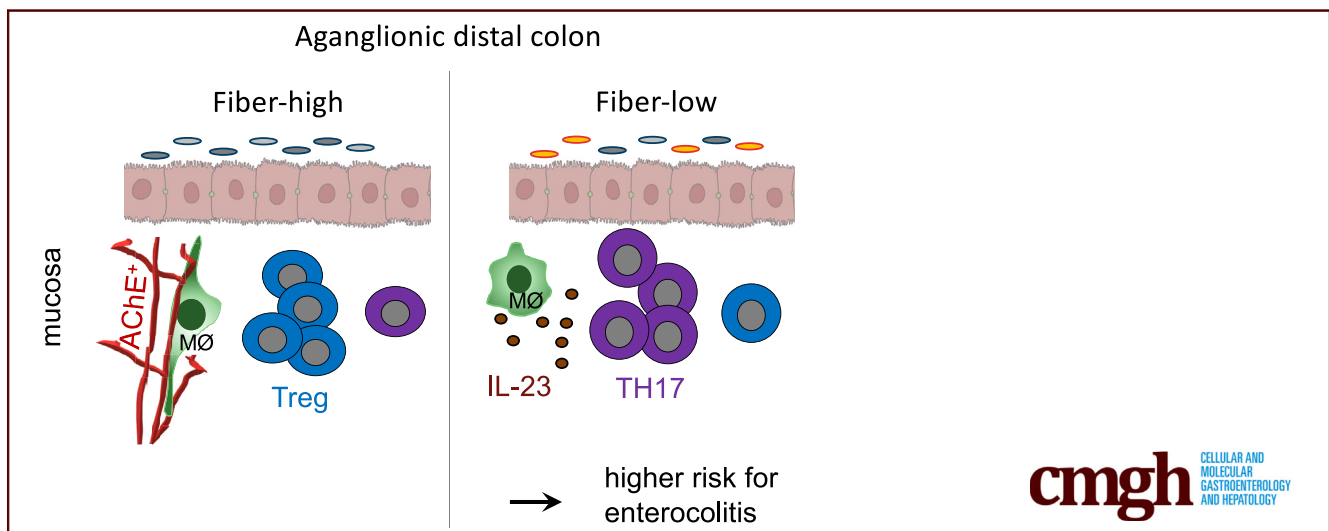
Lack of Mucosal Cholinergic Innervation Is Associated With Increased Risk of Enterocolitis in Hirschsprung's Disease



Simone Keck,¹ Virginie Galati-Fournier,¹ Urs Kym,¹ Michèle Moesch,¹ Jakob Usemann,² Isabelle Müller,¹ Ulrike Subotic,^{1,3} Sasha J. Tharakan,³ Thomas Krebs,⁴ Eleuthere Stathopoulos,⁵ Peter Schmittenebecher,⁶ Dietmar Cholewa,⁷ Philipp Romero,⁸ Bertram Reingruber,⁹ Elisabeth Bruder,¹⁰ NIG Study Group,^{11,12} and Stefan Holland-Cunz¹

¹Department of Pediatric Surgery, University Children's Hospital Basel (UKBB) and University of Basel, Basel, Switzerland;

²Department of Pediatric Pulmonology, University Children's Hospital Basel (UKBB), Basel, and Division of Respiratory Medicine, University Children's Hospital Zurich, Zurich, Switzerland; ³Department of Pediatric Surgery, University Children's Hospital Zurich, Zurich, Switzerland; ⁴Department of Pediatric Surgery, Children's Hospital of Eastern Switzerland, St Gallen, Switzerland; ⁵Department of Pediatric Surgery, University Hospital of Lausanne (CHUV), Lausanne, Switzerland; ⁶Department of Pediatric Surgery, Municipal Hospital, Karlsruhe, Germany; ⁷Department of Pediatric Surgery, University Hospital of Bern, Bern, Switzerland; ⁸Department of Pediatric Surgery, University Hospital of Heidelberg, Heidelberg, Germany; ⁹Department of Pediatric Surgery, Florence Nightingale Hospital, Düsseldorf, Germany; ¹⁰Institute for Medical Genetics and Pathology, University Hospital Basel, Basel, Switzerland; ¹¹NIG Study Group; and ¹²Department of Pathology, University Hospital of Lausanne (CHUV) and University of Lausanne, Lausanne, Switzerland



SUMMARY

Lacking colonic mucosal innervation correlated with increased inflammatory immune cell status, microbial dysbiosis, and higher incidence of postoperative enterocolitis in HSCR patients. Mucosal nerve fibers might serve as a prognostic marker for enterocolitis development and offer new therapeutic intervention strategies.

BACKGROUND & AIMS: Hirschsprung's disease (HSCR) is a congenital intestinal motility disorder defined by the absence of enteric neuronal cells (ganglia) in the distal gut. The development of HSCR-associated enterocolitis remains a life-threatening complication. Absence of enteric ganglia implicates innervation of acetylcholine-secreting (cholinergic) nerve

fibers. Cholinergic signals have been reported to control excessive inflammation, but the impact on HSCR-associated enterocolitis is unknown.

METHODS: We enrolled 44 HSCR patients in a prospective multicenter study and grouped them according to their degree of colonic mucosal acetylcholinesterase-positive innervation into low-fiber and high-fiber patient groups. The fiber phenotype was correlated with the tissue cytokine profile as well as immune cell frequencies using Luminex analysis and fluorescence-activated cell sorting analysis of colonic tissue and immune cells. Using confocal immunofluorescence microscopy, macrophages were identified in close proximity to nerve fibers and characterized by RNA-seq analysis. Microbial dysbiosis was analyzed in colonic tissue using 16S-rDNA gene sequencing. Finally, the fiber phenotype was correlated with postoperative enterocolitis manifestation.

RESULTS: The presence of mucosal nerve fiber innervation correlated with reduced T-helper 17 cytokines and cell frequencies. In high-fiber tissue, macrophages co-localized with nerve fibers and expressed significantly less interleukin 23 than macrophages from low-fiber tissue. HSCR patients lacking mucosal nerve fibers showed microbial dysbiosis and had a higher incidence of postoperative enterocolitis.

CONCLUSIONS: The mucosal fiber phenotype might serve as a prognostic marker for enterocolitis development in HSCR patients and may offer an approach to personalized patient care and new therapeutic options. (*Cell Mol Gastroenterol Hepatol* 2021;12:507–545; <https://doi.org/10.1016/j.jcmgh.2021.03.004>)

Keywords: Enterocolitis; Neuroimmunology; Cholinergic Nerve Fibers; Macrophages; Th17 Cells; Microbiome.

Hirschsprung's disease (HSCR) is a multigenetic congenital malformation of the colon characterized by a distal lack of enteric ganglia cells (aganglionosis) leading to intestinal obstruction and prestenotic megacolon. In affected infants, the aganglionic bowel is surgically removed, and healthy ganglionic tissue is pulled through and reconnected near the anus. Either preoperatively or postoperatively, 20%–50% of patients experience life-threatening HSCR-associated enterocolitis leading to acute abdominal distention, diarrhea, and fever through to sepsis and organ failure.¹ The underlying pathogenesis is not fully understood but appears to involve changes in intestinal barrier function,² immune response,³ and the microbiome.⁴ The absence of ganglia from the distal colon in HSCR is associated with an increase in acetylcholinesterase (AChE) activity concomitant with hypertrophic AChE-positive nerve fibers.^{5–14} AChE degrades the neurotransmitter acetylcholine (ACh), the primary transmitter of the parasympathetic nervous system and a neurotransmitter released by many types of enteric neurons.

Intestinal cholinergic (ACh-producing) signals not only coordinate physiological bowel function but also prevent excessive inflammation by allowing the intestinal immune system to tolerate harmless commensals and food antigens. The cholinergic anti-inflammatory pathway (CAIP) was first described by the Tracey group.¹⁵ In a model of systemic inflammation, vagus nerve (VN) stimulation favored the release of ACh by memory T cells, which in turn bound to $\alpha 7$ -nicotinic ACh receptor ($\alpha 7$ nAChR)-positive splenic macrophages (M Φ) to reduce tumor necrosis factor (TNF)- α production.^{15,16} This concept was confirmed in intestinal inflammation models involving colitis,¹⁷ food allergy,¹⁸ postoperative ileus (POI),¹⁹ and pancreatitis using VN stimulation or pharmacologic targeting of $\alpha 7$ nAChR. In humans, nicotine, which activates nAChRs, has been associated with clinical improvement of ulcerative colitis.²⁰ VN stimulation in Crohn's disease results in amelioration of disease activity and is a subject of ongoing therapeutic evaluation.^{21–23} Contrary to systemic CAIP, intestinal modulation is independent of the spleen and involves direct activation of local enteric neurons.¹⁹ Although VN activation leads to down-regulation of inflammatory cytokine

production by muscularis M Φ (MM Φ) via $\alpha 7$ AChR activation in POI, it remains unclear which receptors and cell types are involved in colitis amelioration. Because the enteric nervous system (ENS) uses more than 30 different neurotransmitters, it is challenging to identify individual immunomodulating functions. Because of the lack of ENS-specific neurotransmitters and the presence of hypertrophic AChE-positive nerve fibers in the aganglionic colon of HSCR patients, neuronal cholinergic function can be examined particularly well.


Here we investigated the association of mucosal cholinergic innervation with immune cell status, microbial composition, and development of postoperative enterocolitis in HSCR patients.

Results

Distinct Mucosal Cholinergic Innervation of the Colon in HSCR Patients

In this prospective, multicenter study, we collected fresh tissue of different colonic segments from 44 pediatric HSCR patients undergoing pull-through surgery as well as 6 control patients (non-HSCR) undergoing surgery for miscellaneous reasons. Compared with non-HSCR colonic tissue, the aganglionic colon of HSCR patients lacks the intrinsic myenteric and submucosal plexus but shows the characteristic increase of AChE activity in the rectosigmoid (Figure 1A). Increased nerve fiber innervation is limited to the aganglionic rectosigmoid colon and decreases in a caudocranial direction.⁵ As a consequence, no mucosal nerve fibers can be detected in the proximal aganglionic descending colon (DC) and only a few in the intermuscular space. Depending on the length of aganglionosis, the proximal DC segment of HSCR patients can be ganglionic, hypoganglionic, or aganglionic (Figure 1A, Table 1). DC segments showing a hypoganglionic phenotype (transition zone) were excluded from the analysis.

Abbreviations used in this paper: ACh, acetylcholine; AChE, acetylcholinesterase; APC, antigen-presenting cell; $\alpha 7$ nAChR, $\alpha 7$ -nicotinic ACh receptor; BMP, bone morphogenetic protein; CAIP, cholinergic anti-inflammatory pathway; CCR2, C-C chemokine receptor type 2; CX3CR1, CX3X chemokine receptor 1; DC, descending colon; ENS, enteric nervous system; EPHB2, ephrin type B-receptor 2; FACS, fluorescence-activated cell sorting; FISH, fluorescence in situ hybridization; Foxp3+, forkhead box P3 positive; GDF, growth/differentiation factor; HSCR, Hirschsprung's disease; Ig, immunoglobulin; IL, interleukin; ILC, innate lymphoid cell; LP, lamina propria; MM Φ , muscle macrophages; M Φ , macrophages; NCR, NK cell receptors; NK, natural killer; NOS, nitric oxide synthase; NRP1, neuropilin-1; OTU, operational taxonomic unit; PBMC, peripheral blood mononuclear cell; PBS, phosphate-buffered saline; PCA, principal component analysis; POI, postoperative ileus; qRT-PCR, quantitative real-time polymerase chain reaction; SEMA, semaphorin; TH, tyrosine hydroxylase; Th17, T-helper 17; Treg, regulatory T cells; TNF, tumor necrosis factor; UNC5B, UNC-5 homology B; VACht, vesicular acetylcholine transporter; VIP, vasoactive intestinal peptide; VN, vagus nerve.

 Most current article

© 2021 The Authors. Published by Elsevier Inc. on behalf of the AGA Institute. This is an open access article under the CC BY-NC-ND license (<http://creativecommons.org/licenses/by-nc-nd/4.0/>).

2352-345X

<https://doi.org/10.1016/j.jcmgh.2021.03.004>

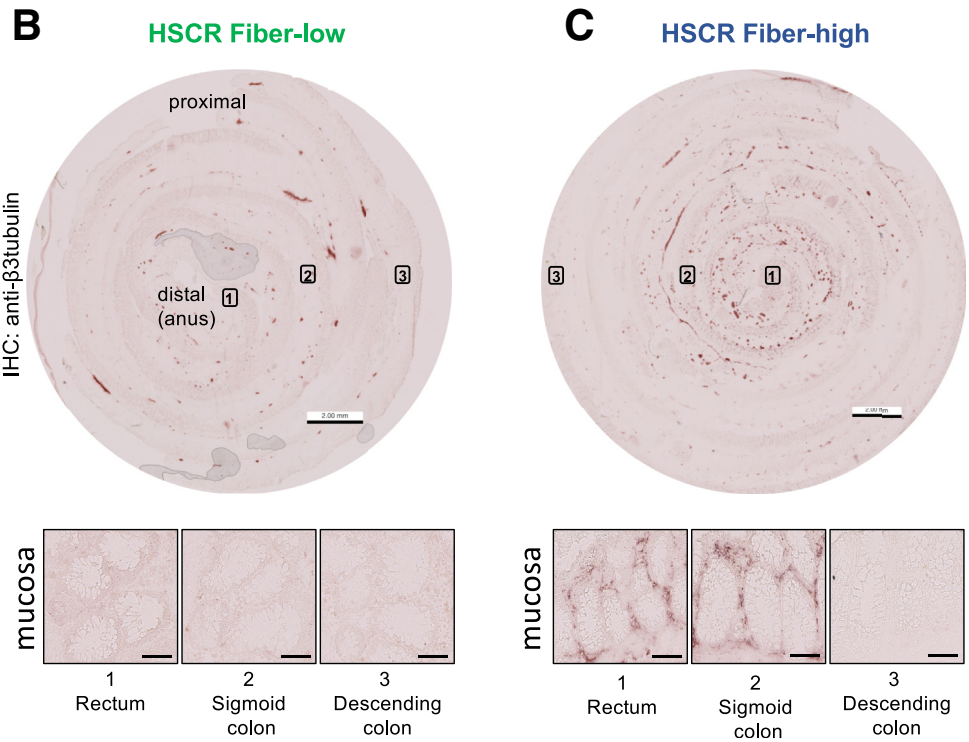
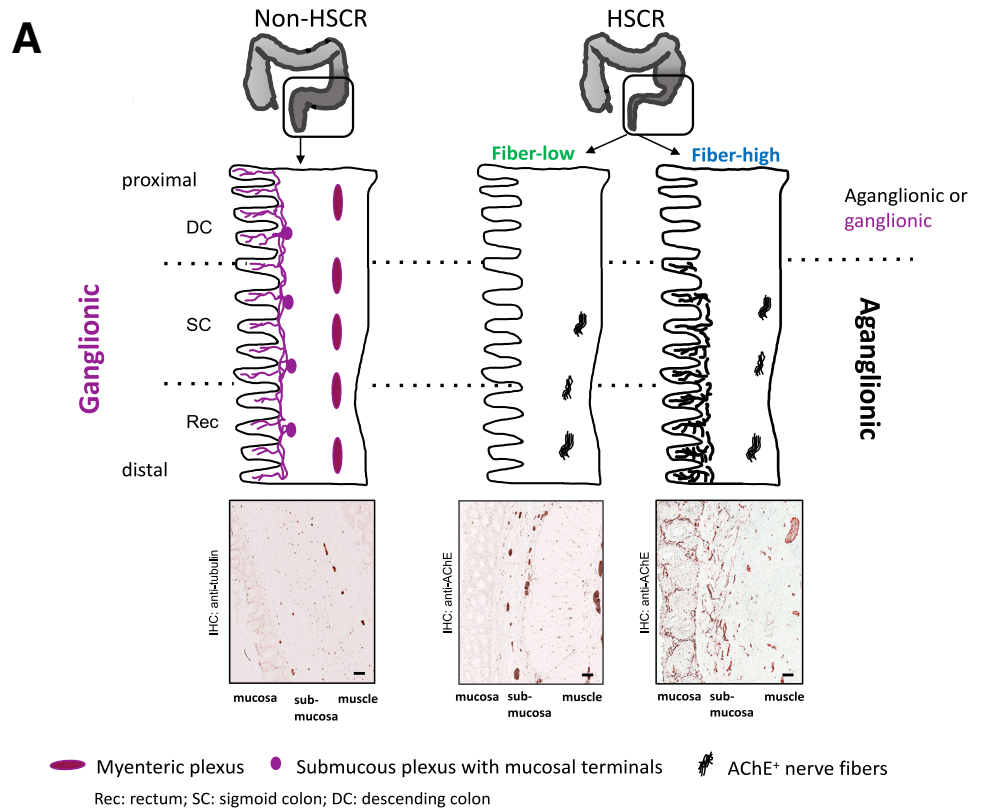


Figure 1. Distribution of neuronal innervation and fiber scoring of HSCR patients. (A) Schematic representation of neuronal innervation in non-HSCR and HSCR patients. Immunohistochemical anti- β 3tubulin staining of ganglionic DC region (non-HSCR) or anti-AChE staining of aganglionic rectum region (HSCR). Scale bar: 50 μ m. (B and C) Anti- β 3tubulin immunohistochemical staining of Swiss roll cryosections from HSCR fiber-low phenotype (B) and fiber-high phenotype (C). Close-up views show mucosal region from 1, rectum; 2, sigmoid colon; and 3, descending colon. Scale bar: 2 mm; Scale bar close-up views: 20 μ m.

We performed anti- β 3tubulin immunohistochemistry staining (pan neuronal marker) in aganglionic cryosections of longitudinally rolled colonic stripes (Swiss roll), including the rectum, sigmoid colon, and DC from HSCR patients.

All patients' tissues showed the typical thick nerve fiber bundles in the colonic muscle region,²⁴ but the density of thin mucosal fibers varied between patients²⁵ (Figure 1B and C). No mucosal nerve fibers could be detected in the aganglionic

Table 1. Overview of Prospective HSCR Patient Cohort

Study number	Sex	Age at surgery (mo)	Operative technique	Site of operation	Diagnosis	Length of AG	Fiber score	DC aganglionic	DC ganglionic	Postoperative clinical symptoms: Obstipation (1); Incontinence (2); Enterocolitis (3); Pain (4)	Postoperative clinical treatment: Laxative (1); Clyster (2); Botox (3); Antibiotics (4); Colonic irrigation (5); Pre-/probiotics (6)
HSCR patients											
0002	F	6.6	abdominal Swenson	01	HSCR	TCA	low	x		1,2,3,4	1,2,4,5,6
0004	M	6.7	transanal Soave	02	HSCR	S-HSCR	low			no	no
0005	M	127.5	transanal Soave	10	HSCR	S-HSCR	low			2,3,4	1,4,5
0006	F	4.3	transanal Soave	10	HSCR	S-HSCR	low			1	1
0010	M	3.9	transanal Swenson	07	HSCR	S-HSCR	high			no	no
0012	M	4.9	transanal Swenson	09	HSCR	L-HSCR	high	x		1	1,2
0013	M	6.9	transanal Swenson	07	HSCR	S-HSCR	low			no	no
0014	M	3.9	transanal Soave	10	HSCR	S-HSCR	low		x	3	4
0015	F	2.8	transanal Soave	01	HSCR	S-HSCR	low		x	no	no
0016	M	3.2	transanal Soave	10	HSCR	S-HSCR	high			no	4
0017	M	5.9	abdominal Soave	09	HSCR	TCA	low	x		no	no
0018	M	3.2	transanal Soave	10	HSCR	S-HSCR	high		x	no	4
0020	M	11.8	transanal Soave	07	HSCR	L-HSCR	low	x		no	no
0021	M	23.5	transanal Soave	04	HSCR	S-HSCR	low			1	2
0022	M	7.2	abdominal Soave	09	HSCR	TCA	low	x		no	4
0023	F	14.2	transanal Soave	04	HSCR	S-HSCR	low		x		
0025	M	3	transanal Soave	10	HSCR	S-HSCR	high		x	no	4
0029	M	10.1	transanal Soave	09	HSCR	L-HSCR	high	x		2,4	no
0032	M	35.9	transanal Soave	04	HSCR	S-HSCR	high		x		
0034	M	2.9	abdominal Soave	06	HSCR	TCA	low	x		no	no
0038	M	19.2	abdominal Soave	10	HSCR	TCA	low	x		no	no
0039	M	12.5	transanal Soave	09	HSCR	S-HSCR	low			4	no
0040	M	3.8	transanal Soave	02	HSCR	S-HSCR	low			no	no
0041	M	5.9	transanal Soave	03	HSCR	L-HSCR	low	x		1	1
0042	M	2.2	transanal Soave	06	HSCR	S-HSCR	low			1,3	1,3,4,5
0044	M	13.6	transanal Soave	03	HSCR	S-HSCR	low		x	no	no
0047	M	44.5	transanal Soave	02	HSCR	S-HSCR	high			2	no
0048	M	3.8	transanal Soave	07	HSCR	S-HSCR	low			1	3,5
0049	M	70.5	transanal Soave	10	HSCR	S-HSCR	low		x	no	4
0050	M	5.7	transanal Soave	10	HSCR	L-HSCR	low			no	no
0051	M	2.5	transanal Soave	08	HSCR	S-HSCR	low			3	no
0053	M	1	transanal Soave	06	HSCR	S-HSCR	low			1,3	1,2,3,4,5

Table 1. Continued

Study number	Sex	Age at surgery (mo)	Operative technique	Site of operation	Diagnosis	Length of AG	Fiber score	DC aganglionic	DC ganglionic	Postoperative clinical symptoms: Obstipation (1); Incontinence (2); Enterocolitis (3); Pain (4)	Postoperative clinical treatment: Laxative (1); Clyster (2); Botox (3); Antibiotics (4); Colonic irrigation (5); Pre-/probiotics (6)
0054	F	6.1	transanal Soave	10	HSCR	S-HSCR	low			no	no
0056	M	4.2	transanal Soave	08	HSCR	S-HSCR	high		x	1	1
0057	F	7.7	transanal Soave	08	HSCR	S-HSCR	high			1,3	1,4,5,6
0058	M	5.7	transanal Soave	08	HSCR	S-HSCR	high		x	3	4,5
0059	M	5	transanal Soave	10	HSCR	S-HSCR	low			no	no
0060	M	5	abdominal Soave	10	HSCR	TCA	high	x		4	5
0061	M	2.8	transanal Soave	02	HSCR	S-HSCR	low			1	1
0063	M	3.8	transanal Soave	08	HSCR	S-HSCR	low		x	3,4	1,4,5
0064	F	64	abdominal Soave	01	HSCR	TCA	low	x		no	4
0065	F	34.5	transanal Soave	09	HSCR	S-HSCR	low			no	no
0066	F	5.3	transanal Soave	01	HSCR	L-HSCR	low	x		no	6
0068	M	3.9	transanal Soave	09	HSCR	S-HSCR	high		x	no	no
Non-HSCR patients											
0024	M	0.4	transabdominal	01	Anal atresia/ Ostomy				x		
0030	M	7	transabdominal	06	Anal atresia/ Ostomy				x		
0037	M	5	transabdominal	01	Anal atresia/ Ostomy				x		
0062	M	5.9	transabdominal	01	Anal atresia/ Ostomy				x		
0067	F	6.8	transabdominal	01	Colonic perforation/ Ostomy				x		
0045	M	11.9	transabdominal	10	Misdiagnosed HSCR				x		

NOTE. Site of operation: Basel 01; Bern 02; Düsseldorf 03; Freiburg 04; Heidelberg 06; Karlsruhe 07; Lausanne 08; St Gallen 09; Zürich 10. Length of aganglionosis (AG): L-HSCR (long-segmented HSCR); S-HSCR (short-segmented HSCR); TCA (total colonic aganglionosis).

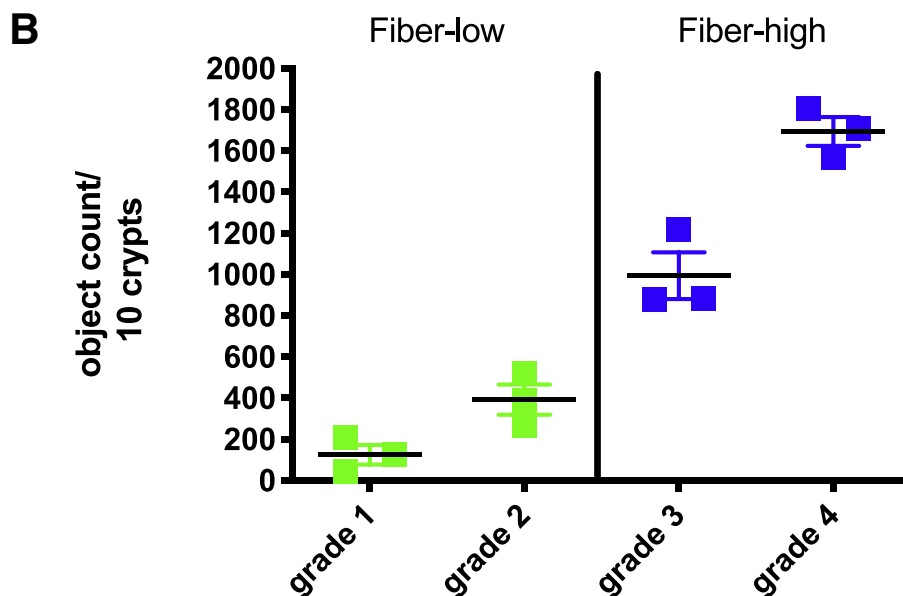
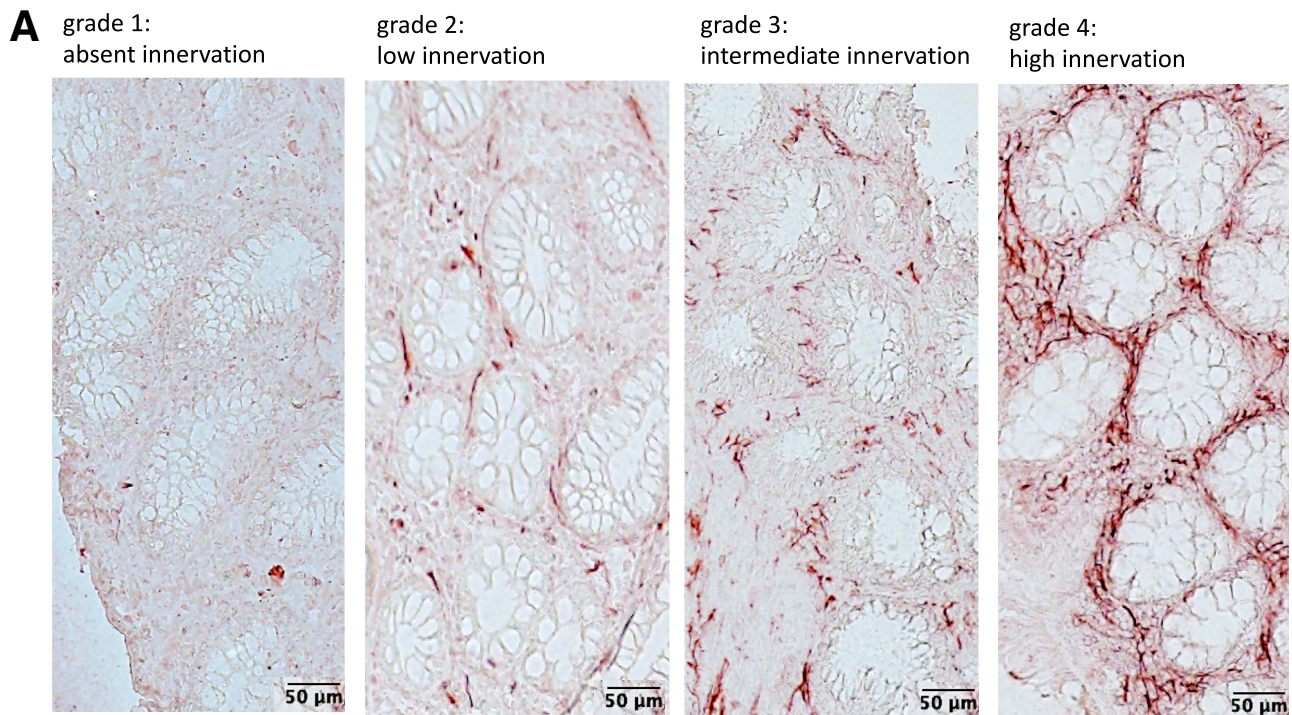


Figure 2. Fiber innervations grades for fiber scoring. (A) AChE immunohistochemistry of 5- μ m cryosections of distal aganglionic colon showing 4 different mucosal innervation grades. Grades 1 and 2 were grouped into fiber-low and 3 and 4 were grouped into fiber-high HSCR patients. (B) Using brightfield microscopy and CellSens Dimension Software, the innervation grade was quantitatively confirmed in 3 representative patients per group. Scatter dot plots show means \pm standard error of the mean. Scale bar: 50 μ m

descending colon (Figure 1B and C). According to mucosal innervation in the distal rectosigmoid colon, the sections were semiquantitatively allocated into low-fiber (Figure 1B) and high-fiber (Figure 1C) patient groups in a double-blind investigation. The fiber innervation grade was quantitatively confirmed in 3 representative patients per group (Figure 2). Fiber phenotype was validated using both anti-AChE and anti- β 3tubulin immunohistochemistry (Figure 3).

Consequently, for further analysis, aganglionic and ganglionic segments with variable mucosal nerve fiber innervation were defined as illustrated by anti- β 3tubulin and anti-AChE immunofluorescent staining (Figure 4A). Thus, rectosigmoid low-fiber tissues were those lacking intrinsic nerve cell bodies as well as mucosal AChE⁺ innervation. Rectosigmoid high-fiber tissues were those lacking intrinsic nerve cell bodies but showing mucosal AChE⁺ innervation

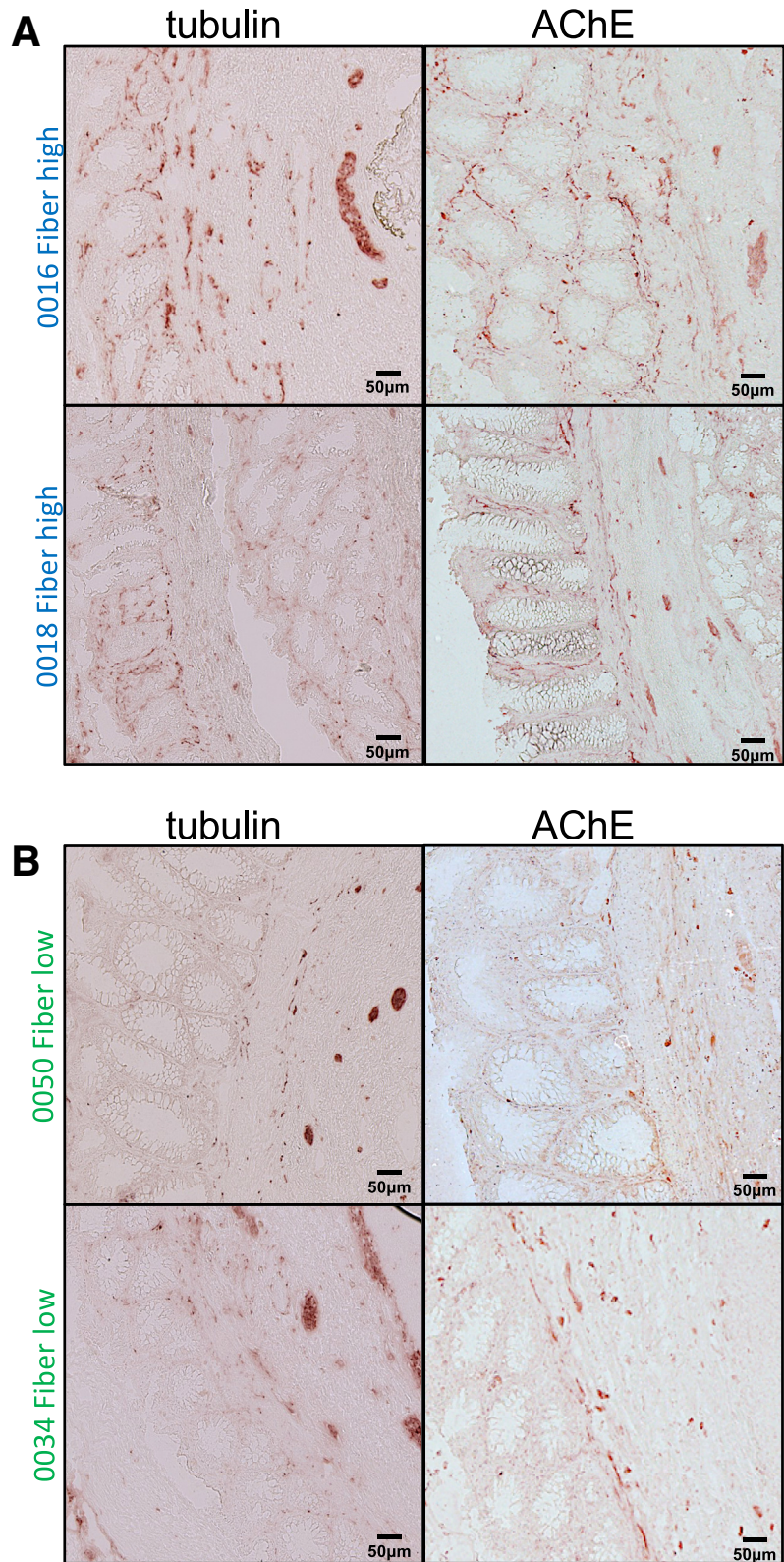


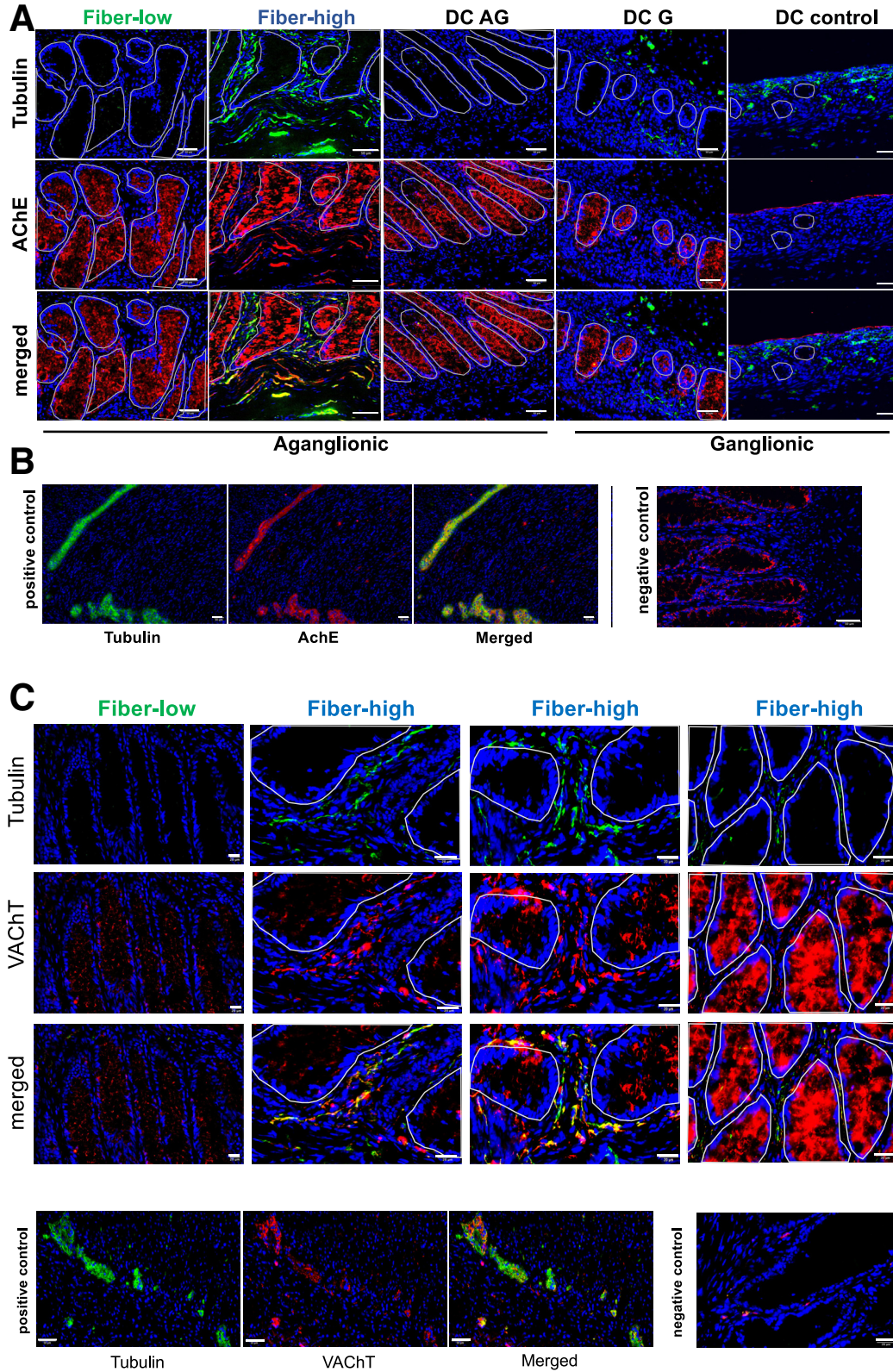
Figure 3. Fiber scoring of distal colon of HSCR patients using tubulin and AChE immunohistochemistry. Tubulin and AChE immunohistochemistry of 5- μ m cryosections of distal aganglionic colon of 2 fiber-high (A) and 2 fiber-low (B) HSCR patients. Scale bar: 50 μ m.

(Figure 4A). Aganglionic DC sections from HSCR patients were defined as those lacking intrinsic nerve cell bodies as well as mucosal AChE⁺ innervation. Ganglionic DC sections from HSCR and non-HSCR patients showed the presence of

AChE⁻ mucosal nerve terminals (Figure 4A) and AChE⁺ nerve cell bodies (ganglia) (Figure 4B, positive control). DC segments (aganglionic and ganglionic) were used from both low-fiber and high-fiber patient tissue.

Former studies reported non-neuronal expression of ACh in intestinal epithelial cells.^{26,27} Although secondary antibody controls showed high unspecific background

signals in the epithelial crypt region (Figure 4B, negative control), a strong epithelial AChE reactivity was detected in some samples (Figure 4A, encircled areas). Using



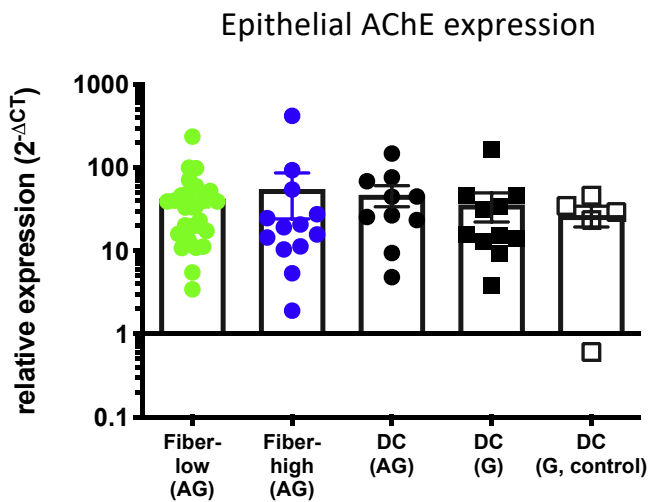


Figure 5. AChE expression in colonic epithelial cells. After tissue digestion colonic epithelial cells were purified from the interphase of 20% and 40% Percoll Gradient. Epithelial cells were immediately lysed, total RNA was isolated, and cDNA was synthesized. Relative gene expression was calculated using the $2^{-\Delta CT}$ method, with $\beta 2$ -microglobulin as the housekeeping gene. Scatter plots with bar show means \pm standard error of the mean. Significance was determined by multiple comparison using one-way analysis of variance. Fiber-low, $n = 27$; fiber-high, $n = 13$; DC (AG), $n = 10$; DC (G), $n = 11$; DC control, $n = 6$. AG, aganglionic; G, ganglionic.

quantitative real-time polymerase chain reaction (qRT-PCR) analysis of purified colonic epithelial cells from HSCR patients and control patients, no significant difference in AChE expression could be observed between the different groups (Figure 5). To confirm a cholinergic origin of the mucosal nerve fibers we performed immunofluorescence staining using tubulin and vesicular acetylcholine transporter (VAcHT), the transporter making ACh available for secretion (Figure 4C). Immunofluorescence studies in high-fiber tissue excluded peptidergic (vasoactive intestinal peptide [VIP]), dopaminergic/adrenergic (tyrosine hydroxylase [TH]), and nitrinergic (nitric oxide synthase [NOS]) origins of the mucosal fibers and demonstrated that the majority of mucosal fibers were not associated with the glia cell marker S100B (Figure 6A). All markers were expressed in myenteric ganglia from ganglionic DC tissue (Figure 6B).

We did not observe any significant patient bias in terms of anthropometric, clinical, environmental, or maternal

factors between low-fiber and high-fiber tissues, except a higher percentage of infants delivered by cesarean section in the high-fiber patient group (Table 2).

Absence of Neuronal Signals Correlated With Inflammatory Immune Status

A functional ENS is crucial for intestinal immune homeostasis. To investigate whether the absence of enteric neuronal cells and/or nerve fibers correlated with impaired inflammatory cytokine status in HSCR patients, we performed Luminex (Austin, TX) analysis of full-thickness colonic tissue (mucosa, submucosa, muscle) from HSCR patients and control patients.

Interleukin (IL) 17 was significantly less abundant in mucosal innervated high-fiber tissue samples compared with aganglionic DC samples (Figure 7A). In aganglionic DC samples, IL6 and IL1 β were increased compared with ganglionic DC samples as well as aganglionic high-fiber samples. IL22, IL23, and interferon- γ proteins were comparably expressed in the different groups, whereas TNF- α was significantly elevated in aganglionic compared with ganglionic HSCR DC samples (Figure 7A). In summary, we found elevated levels of inflammatory cytokines in aganglionic DC samples lacking enteric neurons as well as AChE⁺ nerve fibers. This elevation was decreased in ganglionic DC samples for IL6 and IL1 β and in aganglionic high-fiber samples for IL17, IL6, and IL1 β , all of which are involved in CD4 Ror γ T⁺ T-helper 17 (Th17) cell differentiation and effector function.

Beside innate lymphoid cells (ILC) 3 and others, Th17 cells are the main producers of IL17 and are counter-regulated by forkhead box P3 positive (Foxp3⁺) regulatory T cells (Treg). Frequencies of mucosal IL17⁺, Th17, and Foxp3⁺ Treg T cells were assessed by flow cytometry. Th17 frequencies were significantly increased in low-fiber segments compared with high-fiber segments or DC segments (Figure 7B, Figure 8A). We observed no difference between aganglionic and ganglionic DC tissue of HSCR and control patients. Foxp3⁺ Treg cell frequencies were significantly elevated in cholinergic innervated high-fiber tissues compared with aganglionic and ganglionic DC samples (Figure 7C). Accordingly, the ratio of Th17/Treg cell frequencies was significantly higher in low-fiber segments compared with high-fiber segments (Figure 7D). Frequencies of natural killer (NK) cell receptors (NCR)⁺ and NCR⁻ ILC3 were comparable between the different colonic

Figure 4. (See previous page). Cholinergic innervation in distal colon of HSCR patients. (A) Immunofluorescence of epithelial/mucosal region from aganglionic and ganglionic colonic tissue from HSCR and control patients using tubulin (Alexa647, green) and AChE (Cy3, red). DAPI (blue) shows cell nuclei. Encircled areas mark the epithelial crypt/lumen. Scale bar: 50 μ m. DC AG: aganglionic descending colon; DC G: ganglionic descending colon; DC control: ganglionic descending colon from control patients. (B) Positive control: immunofluorescence of myenteric plexus ganglia from ganglionic control tissue. Negative control: immunofluorescence of epithelial/mucosal region from aganglionic fiber-high colonic tissue using secondary antibody controls mouse IgG2b-biotin/SA-Cy3 together with mouse IgG2a-A647. Scale bar: 50 μ m. (C) Immunofluorescence of epithelial/mucosal region from aganglionic fiber-low and fiber-high colonic tissue from HSCR patients using tubulin (Alexa647, green) and VAcHT (A555, red). DAPI (blue) shows cell nuclei. Encircled areas mark the epithelial crypt/lumen. Positive control: immunofluorescence of myenteric plexus ganglia from ganglionic control tissue. Scale bar: 50 μ m. Negative control: immunofluorescence of epithelial/mucosal region from aganglionic fiber-high colonic tissue using secondary antibody controls mouse IgG1-A555 together with mouse IgG2a-A647. Scale bar: 20 μ m.

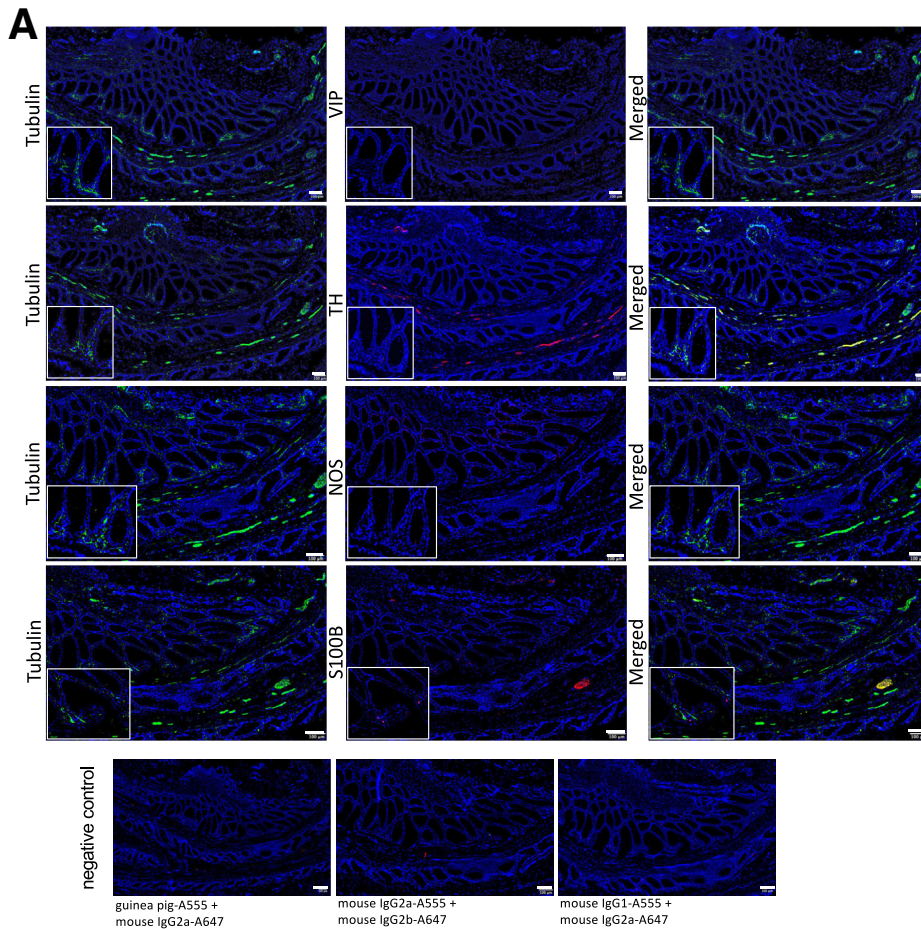
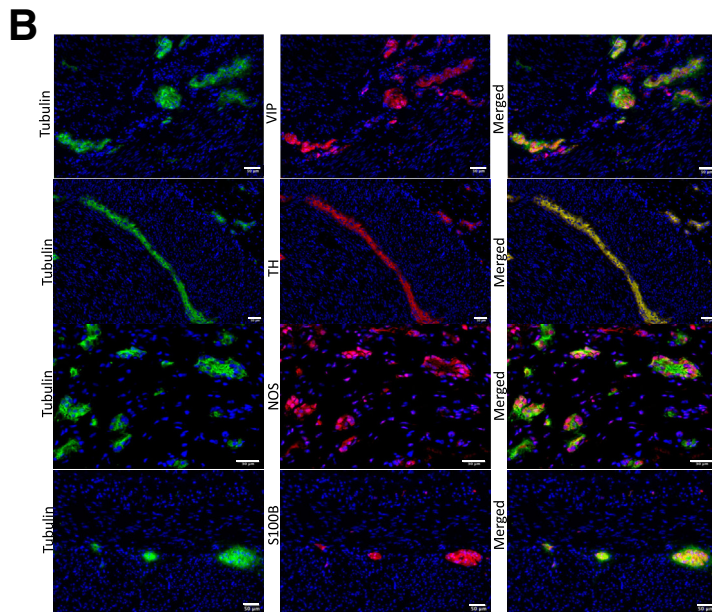


Figure 6. Immunofluorescence analysis of fiber-high HSCR tissue for neuronal marker. (A) Immunofluorescence (5- μ m Swiss roll cryosections) of aganglionic rectum region from a fiber-high patient using tubulin (Alexa647, green), a general neuronal marker, combined with VIP (A555, red), labeling peptidergic neurons; TH (A555, red), labeling dopaminergic and adrenergic neurons; NOS (A555, red), labeling nitrinergic neurons, and S100B (S100 calcium-binding protein B; A555, red), labeling glia cells. DAPI (blue) shows cell nuclei. Images were taken by fluorescence microscopy (original magnification, $\times 20$; scale bar, 100 μ m) and processed by Fiji software. Close-up views (white boxes) show mucosal/epithelial region. Negative control: immunofluorescence (5- μ m Swiss roll cryosections) of aganglionic rectum region from a fiber-high patient using secondary antibody controls. (B) Immunofluorescence of myenteric plexus ganglia from ganglionic control tissue using the antibody combinations from (A). Scale bar, 50 μ m; scale bar for NOS images, 30 μ m.



samples (Figure 8B). Thus, the lack of mucosal nerve fiber innervation in distal low-fiber tissue is associated with increased Th17 cell frequencies and a higher ratio of Th17/Treg cell frequencies.

CX3C chemokine receptor 1⁺ (CX3CR1⁺) M Φ represent the major antigen-presenting cell (APC) type in the colon and are crucial for CD4 T-helper cell differentiation. These M Φ exhibit a non-inflammatory M2-like phenotype and are

Table 2. Characteristics of Prospective HSCR Patient Cohort

Anthropometric data and potential risk factors (no. of patients followed up)	No. patients positive for risk factor/ available patient data (%)	Fiber-low (n = 31)	Fiber-high (n = 13)	P value
Age at operation, mo (n = 44)	5 [1–127]	5 [1–127]	4 [3–44]	.678
Sex, male (n = 44)	35/44 (80)	23 (74)	12 (92)	.174
Preterm birth (n = 40)	3/40 (8)	1 (4)	2 (18)	.114
Pets (n = 41)	13/41 (32)	9 (33)	4 (33)	1.000
Patient living in rural area (n = 42)	21/42 (50)	15 (50)	6 (50)	1.000
Antibiotic treatment (n = 40)	5/40 (13)	4 (15)	1 (8)	.602
Siblings (n = 41)	32/41 (78)	21 (72)	11 (92)	.175
Breastfed at operation (n = 41)	38/41 (93)	27 (90)	11 (100)	.276
Maternal age at delivery, y (n = 37)	28 [21–43]	30 [23–43]	28 [21–35]	.111
Parental smoking (n = 40)	9/40 (13)	5 (18)	4 (33)	.283
Cesarean section (n = 40)	14/40 (35)	7 (25)	7 (58)	.043
Maternal allergy (n = 40)	11/40 (28)	7 (25)	4 (33)	.685

NOTE. Values are median [range] or number (percentage %).

essential for local expansion and maintenance of Treg.²⁸ In contrast, intestinal C-C chemokine receptor type 2⁺ (CCR2) CX3CR1 blood-monocyte-derived MΦ are essential for Th17 cell differentiation.^{29,30} We performed qRT-PCR analysis in full-thickness and colonic muscle tissue to check for expression of CX3CR1 and CCR2. In high-fiber tissue as well as in colonic muscle tissue, we found a significantly higher expression of CX3CR1 than CCR2, whereas in all other segments expression levels of the 2 markers were comparable (Figure 8C). We next investigated viable CD64⁺ MΦ by flow cytometry. All MΦ expressed comparable levels of CD11c (Figure 7E). However, we found a significantly higher expression of CD14, an M2 marker,³¹ in MΦ isolated from the mucosal lamina propria (LPMΦ) of high-fiber colonic tissue and in MΦ isolated from MMΦ (Figure 7E). MMΦ interact with neurons of the myenteric plexus and have been described as bipolarly shaped.^{32–34} Using confocal fluorescence microscopy, we visualized the bipolar shape of LPMΦ in high-fiber segments similar to that seen with MMΦ (Figure 7F, left and right images). In contrast, LPMΦ in low-fiber colonic segments exhibited a round or stellate phenotype (Figure 7F, middle image). We found a significantly higher percentage of bipolar MΦ in high-fiber colonic tissue (Figure 7F, bar graph).

We attempted to mimic the phenotype of the 2 colonic macrophage populations by differentiating blood-derived monocytes from healthy adult donors into M1 and M2 MΦ. After 10 days of differentiation, M2 MΦ showed an elongated bipolar shape (Figure 8D and E) and increased expression of CD14 and CX3CR1 (Figure 8F and G). In contrast, M1 MΦ exhibited a rounded shape and expressed moderate levels of CD14 while lacking CX3CR1 expression. To test the ability of the MΦ to differentiate T cells into certain effector T cells, we co-cultured M1 and M2 MΦ with autologous naive CD4 T cells in the presence of anti-CD3 and performed a Th17 and Treg T-cell differentiation assay. After 6 days of co-culture, the frequency of Th17 and Treg cells was analyzed, and the ratio was calculated. Th17/

Treg ratio was significantly lower when co-cultured with bipolar CX3CR1⁺ CD14^{high} M2 MΦ (Figure 8H). These observations suggested that high-fiber segments of HSCR colon harbor mainly a bipolar CD64⁺ CD11c⁺ CD14^{high} MΦ population in the mucosa possibly associated with decreased Th17 cell frequencies.

Bipolar CD14^{high} MΦ Co-localized With AChE⁺ Nerve Fibers

Both MΦ and T cells express receptors for neurotransmitters, qualifying them for neuronal interaction.^{19,32,33,35,36} Representative fluorescence images (20× and 63×) of high-fiber and low-fiber rectosigmoid colonic tissue revealed CD64⁺ MΦ and CD3⁺ T cells in close proximity to AChE⁺ fibers (Figure 9A). In the colonic muscle layer, MΦ were detected between fasciculated AChE⁺ fiber bundles. To determine which cell type could physically interact with thin mucosal nerve fibers, we performed fast-scanning confocal imaging using a Fiji software macro to determine the sum of overlapping pixel values (Figure 9B, Supplementary Video 1). Per patient (low-fiber segments, n = 4; high-fiber segments, n = 5; muscle, n = 2), 100–200 CD64⁺ or CD3⁺ cells were annotated, and the sum of overlapping AChE⁺ pixel values was determined. The results showed that AChE⁺ fibers in high-fiber tissue as well as colonic muscle segments preferentially co-localized with CD64⁺ LPMΦ in contrast to CD3⁺ T cells (Figure 9C). Using triple immunofluorescence staining against CD64, AChE, and tubulin, we showed that LPMΦ from high-fiber tissue were associated with neuronal tubulin⁺ AChE⁺ fibers rather than non-neuronal tubulin[−] AChE⁺ cells (Figure 10A and B). LPMΦ from ganglionic DC tissue from HSCR and control patients seemed to be associated with tubulin⁺ AChE[−] neurons (Figure 10B), which is consistent with recent reports.^{33,37} These results suggested that bipolar LPMΦ were closely associated with thin mucosal AChE⁺ fibers in aganglionic high-fiber tissue from HSCR patients.

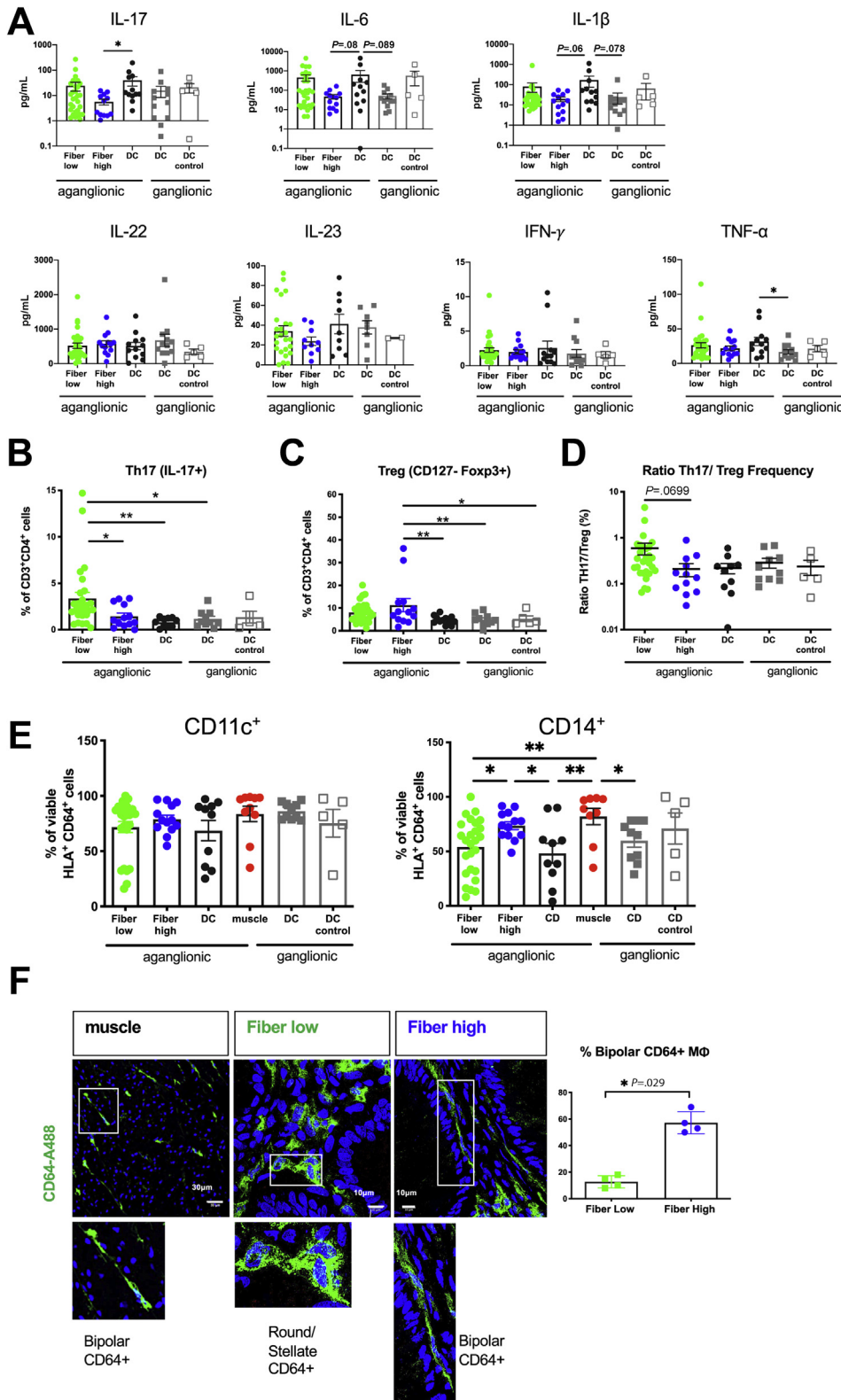


Figure 7. Cytokine profile and immune cell status in colon of HSCR patients. (A) Luminex analysis of full-thickness colonic tissue isolated from different aganglionic (AG) and ganglionic (G) colonic segments of HSCR and control patients. IL23 was determined by enzyme-linked immunosorbent assay. Fiber-low (n = 30); fiber-high (n = 13); AG DC (n = 12); G DC (n = 12); control DC (n = 5). IL23 protein expression was not detectable in 5 fiber-low, 3 fiber-high, 3 aganglionic DC, 5 ganglionic DC, and 3 control DC samples. (B–E) FACS analysis of mononuclear cells isolated from different aganglionic and ganglionic colonic segments of HSCR and control patients. Frequencies of IL17 $^{+}$ Th17 T cells (B), CD127 $^{-}$ Foxp3 $^{+}$ Treg cells (C). Fiber-low (n = 30); fiber-high (n = 13); AG DC (n = 10); G DC (n = 10); control DC (n = 5). (D) Ratio Th17/Treg cells. (E) Frequencies of CD11c $^{+}$ and CD14 $^{+}$ M Φ . Fiber-low (n = 26); fiber-high (n = 13); AG DC (n = 10); muscle (n = 10); G DC (n = 10); control DC (n = 5). (F) Immunofluorescence of CD64 $^{+}$ M Φ from a colonic muscle region (left), a mucosal region from a fiber-low patient (center), and a mucosal region from a fiber-high patient (right). Scale bar: 10 μ m and 30 μ m (muscle). Images from 3 fiber-high and 3 fiber-low patients were analyzed for M Φ shape. A total of 100–200 CD64 $^{+}$ cells per patient were counted, and the percentage of bipolar cells was calculated (bar graph). Scatter plots (with and without bars) show means \pm standard error of the mean. Significance was determined using one-way analysis of variance multiple comparison analysis (A–F) and an unpaired nonparametric Mann-Whitney test (* $P \leq .05$; ** $P \leq .01$; *** $P \leq .001$). Table 10 shows P values. Figure 15 shows the FACS gating strategy.

LPM Φ Isolated From High-Fiber Colonic Tissue Express Diminished IL23 Levels

To identify specific genes potentially targeted by neuronal interaction, we performed RNA sequencing in

viable fluorescence-activated cell sorting (FACS)-sorted mucosal M Φ (CD45 $^{+}$ HLA $^{+}$ CD64 $^{+}$) isolated from low-fiber and high-fiber tissues. As control, we included MM Φ as well as in vitro-differentiated blood-derived M1 and M2 M Φ .

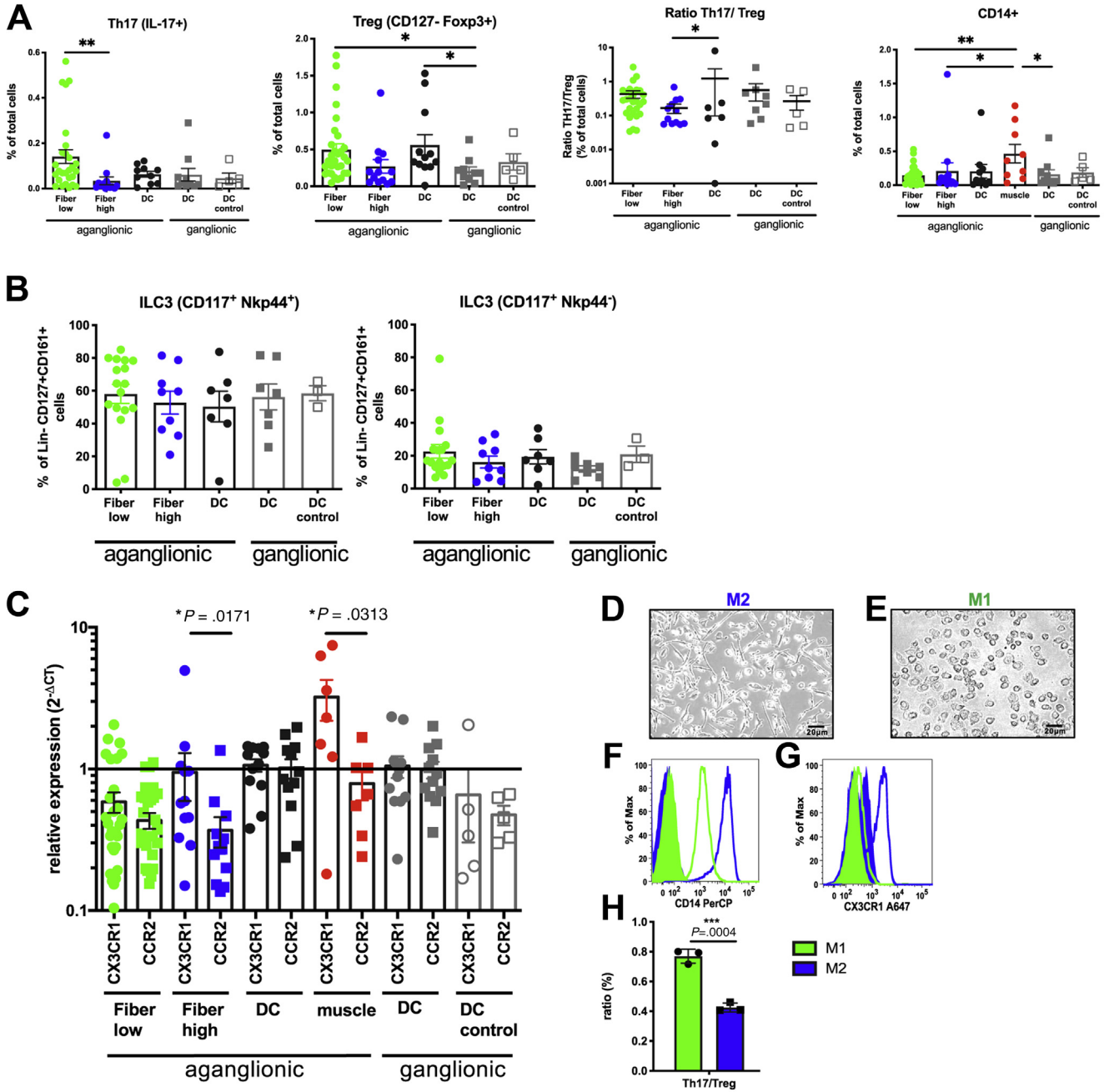
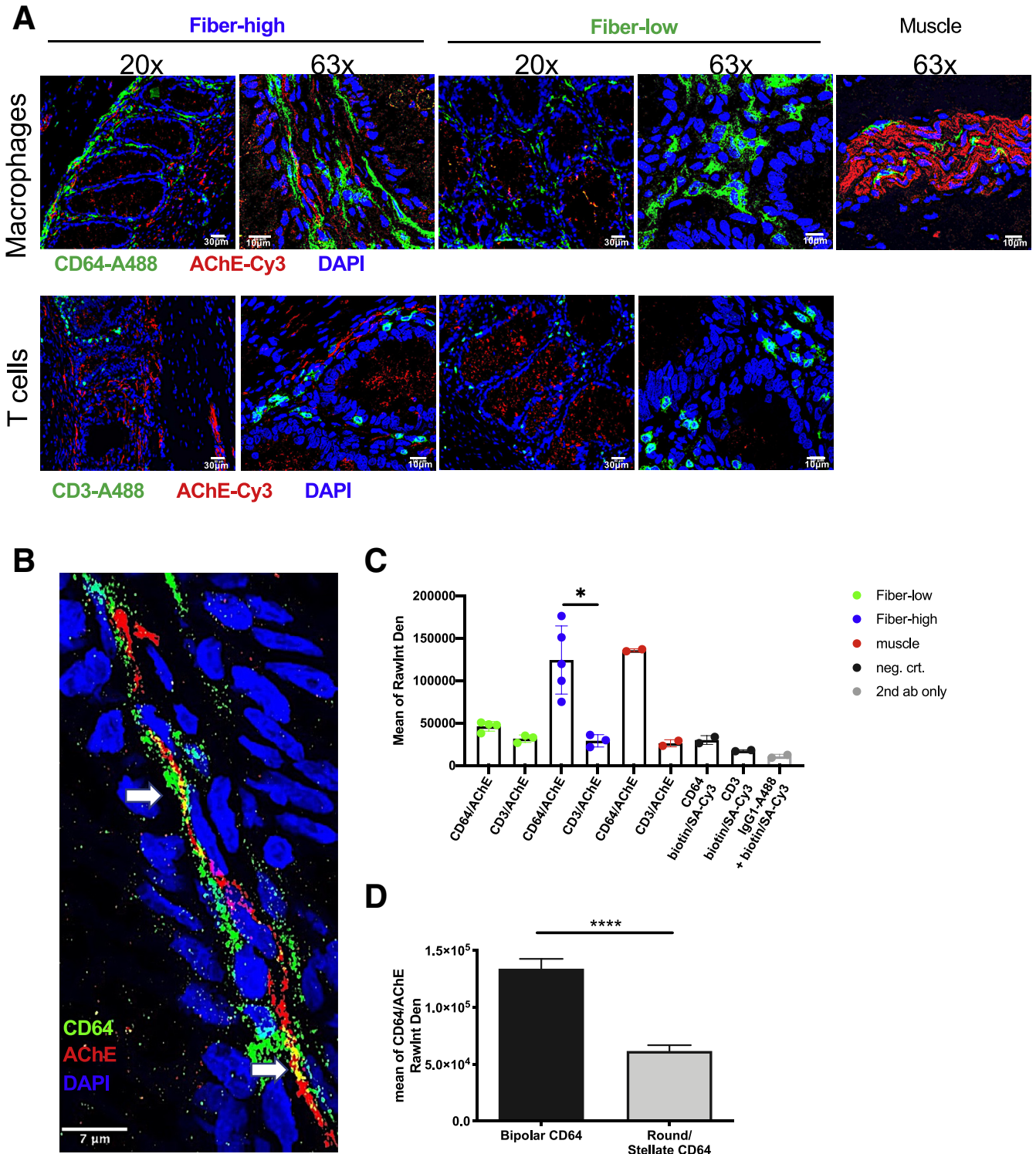


Figure 8. Immune cell populations in colonic tissue from HSCR and control patients and in vitro T-cell conversion assay. (A) Flow cytometric analysis of mononuclear cells isolated from different aganglionic and ganglionic colonic segments of HSCR and control patients. Frequencies of total cells are shown. IL17⁺ Th17 T cells were gated in viable CD3⁺ CD4⁺ lymphocytes restimulated with PMA/ionomycin. Treg cells were defined as CD127⁻ Foxp3⁺ cells in unstimulated viable CD3⁺ CD4⁺ lymphocytes. Fiber-low (n = 30); fiber-high (n = 13); AG DC (n = 10); G DC (n = 10); control DC (n = 5). CD14⁺ MΦ were gated in viable HLA⁺ CD64⁺ cells. Fiber-low (n = 26); fiber-high (n = 13); AG DC (n = 10); muscle (n = 10); G DC (n = 10); control DC (n = 5). Exact P values indicated in Table 10. (B) Frequencies of NCR⁺ (Nkp44⁺) and NCR⁻ (Nkp44⁻) ILC3 (CD117⁻) subsets. Fiber-low (n = 17); fiber-high (n = 9); AG DC (n = 6); G DC (n = 6); control DC (n = 3). Figure 15 shows flow cytometric gating strategy. Scatter plots with bar show means ± standard error of the mean. Significance was determined by multiple comparison using one-way analysis of variance (*P ≤ .05; **P ≤ .01, ***P ≤ .001, ****P ≤ .0001); exact P values indicated in Table 10. (C) Quantitative RT-PCR analysis of full-thickness colonic tissue or isolated muscle tissue from different aganglionic and ganglionic colonic segments of HSCR and control patients (CX3CR1, circles and CCR2, squares). Significance was determined by using Wilcoxon matched-pairs signed-rank test. Fiber-low (n = 31); fiber-high (n = 13); AG DC (n = 12); G DC (n = 11); control DC (n = 5). (D and E) Representative brightfield microscopic images (original magnification, ×10) of M2 (D) and M1 (E) after 10 days of differentiation. Scale bar: 20 μm. (F and G) Flow cytometric analysis of blood-derived M1 and M2 macrophages from adult healthy donors. Histograms show CD14 (F) and CX3CR1 (G) expression in M1 (green) and M2 (blue) macrophages as well as in unstained controls (filled histograms). Representative analysis out of 3 independent experiments is shown. (H) Th17 and Treg conversion assay using blood-derived M1 and M2 macrophages. Frequencies of Th17 and Treg cells were determined, and Th17/Treg ratio was calculated. One out of 3 independent experiments is shown. Significance was determined using unpaired t test. Figure 15 indicates FACS gating strategy.

Principal component analysis (PCA) showed transcriptional separation of blood-derived MΦ from colonic patient-derived MΦ (Figure 11A). Macrophage-specific genes (CD64, CD14, ITGAM, CX3CR1, CCR2, ITGAX, and CSF1R) were similarly expressed between colonic populations, whereas MMΦ expressed muscle-specific Lyve1

(Figure 11B).³⁸ When testing for gut-specific M2 markers (AhR, CD200R1, AREG, CD209, TGF-β2, and IL10), we found elevated expression in colonic subsets similar to blood-derived M2 MΦ. In contrast to LPMΦ from low-fiber segments, LPMΦ from high-fiber tissue as well as MMΦ showed, by trend, decreased expression of chemokine



receptor CCR7 crucial for lymph node homing, indicating a tissue-resident population (Figure 11B). Differential gene expression analysis yielded 24 significantly changed genes between LPM Φ isolated from low-fiber and high-fiber colonic tissues (Figure 11C and D). Strikingly, IL23a, a subunit of the Th17-inducing cytokine IL23, was significantly lower in LPM Φ isolated from high-fiber compared with low-fiber segments. We found a lower expression of IL6 and CCL-20, both of which are involved in Th17 differentiation and recruitment, but comparable TNF- α expression in LPM Φ isolated from high-fiber compared with low-fiber segments (Figure 11E).

Using immunofluorescence analysis, we quantitatively analyzed IL23 protein expression in CD64⁺ LPM Φ in cryosections from low-fiber and high-fiber colonic tissue (Figure 11F and G). LPM Φ in 4–8 regions per patient were analyzed and quantified using CellProfiler software. Low-fiber colonic tissue showed significantly increased frequencies of IL23-positive LPM Φ compared with high-fiber colonic tissue (Figure 11H).

This result suggested that LPM Φ isolated from cholinergic innervated high-fiber colonic tissue exhibited an anti-inflammatory, tissue-resident phenotype with decreased expression of the Th17-inducing cytokine IL23 compared with LPM Φ isolated from low-fiber tissue. Of note, RNA-seq analysis was limited by low sample numbers and high variance and thus needs further validation.

Distinct Expression of Macrophage-Specific Transcripts

Next, we aimed to identify receptors and proteins possibly involved in the neuronal modulation of LPM Φ . On the basis of transcriptional analysis of FACS-sorted mucosal M Φ , we verified the expression of receptors for neurotransmitters, neuropeptides, neurotrophic factors, and axon-guidance proteins (Figure 12). We found a tendency toward elevated levels of nicotinic (CHRNA7, CHRNA5, CHRNA1) and muscarinic (CHRM3) receptors in LPM Φ isolated from high-fiber compared with LPM Φ isolated from low-fiber HSCR tissue (Figure 12A and F). In contrast, other receptors reported to be involved in cholinergic immune suppression such as receptors for serotonin,³⁹ catecholamine (ADRB2),³³ or neuropeptides (NMUR1, VIPR1, SSTR2, and CALCRL)^{40–43} were either not up-regulated in high-fiber

LPM Φ compared with low-fiber LPM Φ or not expressed (Figure 12B, C, and F).

M Φ secrete different neurotrophic and axon-guidance proteins as well as respective receptors. LPM Φ isolated from high-fiber colonic tissue expressed growth/differentiation factor (GDF) 15 and, to a lesser extent, GDF11 (Figure 12D and F). Within the family of axon-guidance proteins, we found elevated expression of the receptors neuropilin-1 (NRP1), UNC-5 homology B (UNC5B), and ephrin type B-receptor 2 (EPHB2) binding semaphorin 3A (SEMA3A), netrin, and ephrin-B family members, respectively. In contrast, LPM Φ isolated from low-fiber segments showed elevated expression of SEMA3A and SEMA7A compared with LPM Φ originating from high-fiber segments (Figure 12E and F).

These data suggested a possible involvement of nicotinic and muscarinic AChRs in neuronal M Φ crosstalk. However, data analysis was limited by low sample numbers and high variance and thus needs further validation.

Microbial Dysbiosis in Colonic Low-Fiber Tissues From HSCR Patients

Lacking intestinal M Φ or ENS affects the composition of intestinal microbiome. In a chemically induced colitis model in mice, CX3CR1⁺ M Φ were crucial to maintain the intestinal barrier function to prevent bacterial translocation.⁴⁴ To evaluate whether the presence of mucosal nerve fibers correlated with altered passage of luminal bacteria through the epithelium into the underlying tissue, we performed bacteria-specific 16S rRNA fluorescence in situ hybridization (FISH) analysis of low-fiber and high-fiber cryosections. EUB338⁺ DAPI⁺ bacteria were detected in the mucosa of both groups, but no significant difference was found (Figure 13A and B). We analyzed the expression of the tight junction proteins occludin and ZO-1 in isolated epithelial cells from HSCR and control patients using qRT-PCR. The coordinated interaction of those proteins is critical for the assembly and maintenance of an effective epithelial barrier. We showed that neither occludin nor ZO-1 was differentially expressed in the diverse groups, suggesting no impact on epithelial permeability between low-fiber and high-fiber colonic tissue (Figure 13C). We then checked the composition of microbial communities by 16S rDNA sequencing in cryosections of low-fiber, high-fiber, and ganglionic DC

Figure 9. (See previous page). CD64⁺ LPM Φ co-localize with AChE⁺ fibers. (A) Immunofluorescence of epithelial region in cryosections of representative fiber-high and fiber-low patients. Anti-AChE (red); anti-CD64 or anti-CD3 (green); DAPI (blue). Scale bar: 10 μ m (original magnification, \times 63 images) and 30 μ m (original magnification, \times 20 images). (B) Confocal immunofluorescence image of an intercrypt region from a fiber-high patient. Overlapping pixels (yellow, arrows) were visualized on a Z-projection image. Scale bar: 7 μ m. See [Supplementary Video 1](#). (C) Quantification of pixel intensity of CD64⁺ M Φ and AChE or CD3⁺ T cells and AChE using a Fiji software macro. Confocal images from rectosigmoid colon regions of fiber-low (n = 4 for CD64; n = 3 for CD3) and fiber-high (n = 5 for CD64; n = 3 for CD3) patients as well as from colonic muscle regions of HSCR patients (n = 2) were taken. The following negative staining controls were used: CD64-A488 or CD3-A488 with biotin + streptavidin-Cy3 and IgG1-A488 + biotin/streptavidin-Cy3 (n = 2). Per patient (dot), 200–300 cells were analyzed. Scatter plots with bar show mean raw integrated density (RawIntDen) \pm standard error of the mean. Significance between CD64/AChE and CD3/AChE within a group was determined using an unpaired nonparametric Mann-Whitney test. (D) CD64⁺ M Φ from 3 fiber-high patients were investigated with respect to bipolar (n = 170) or round/stellate (n = 152) morphologic phenotype. Raw integrated density of co-localized pixels between CD64 and AChE are shown. Significance was determined using an unpaired nonparametric Mann-Whitney test (****P \leq .0001).

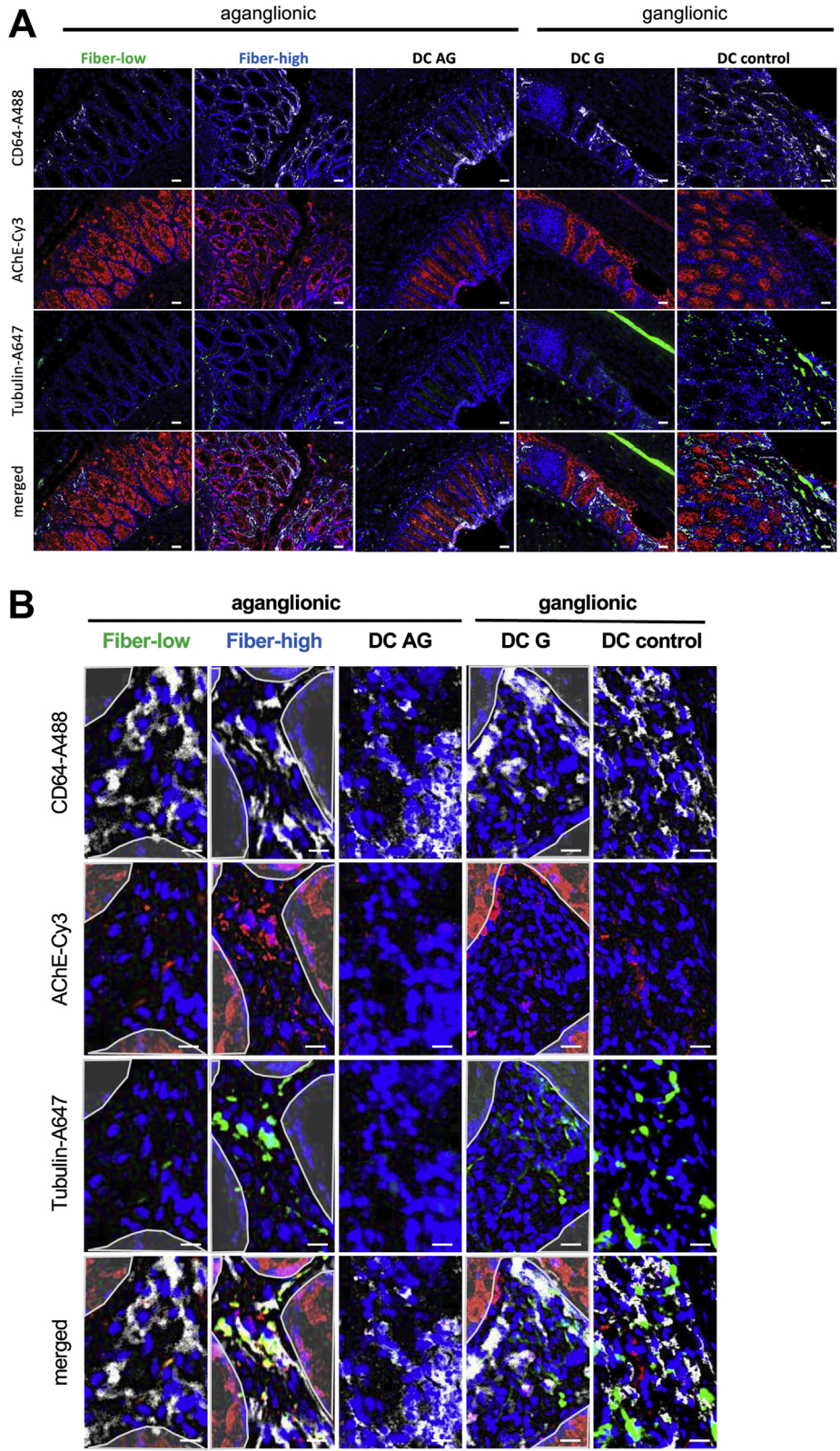


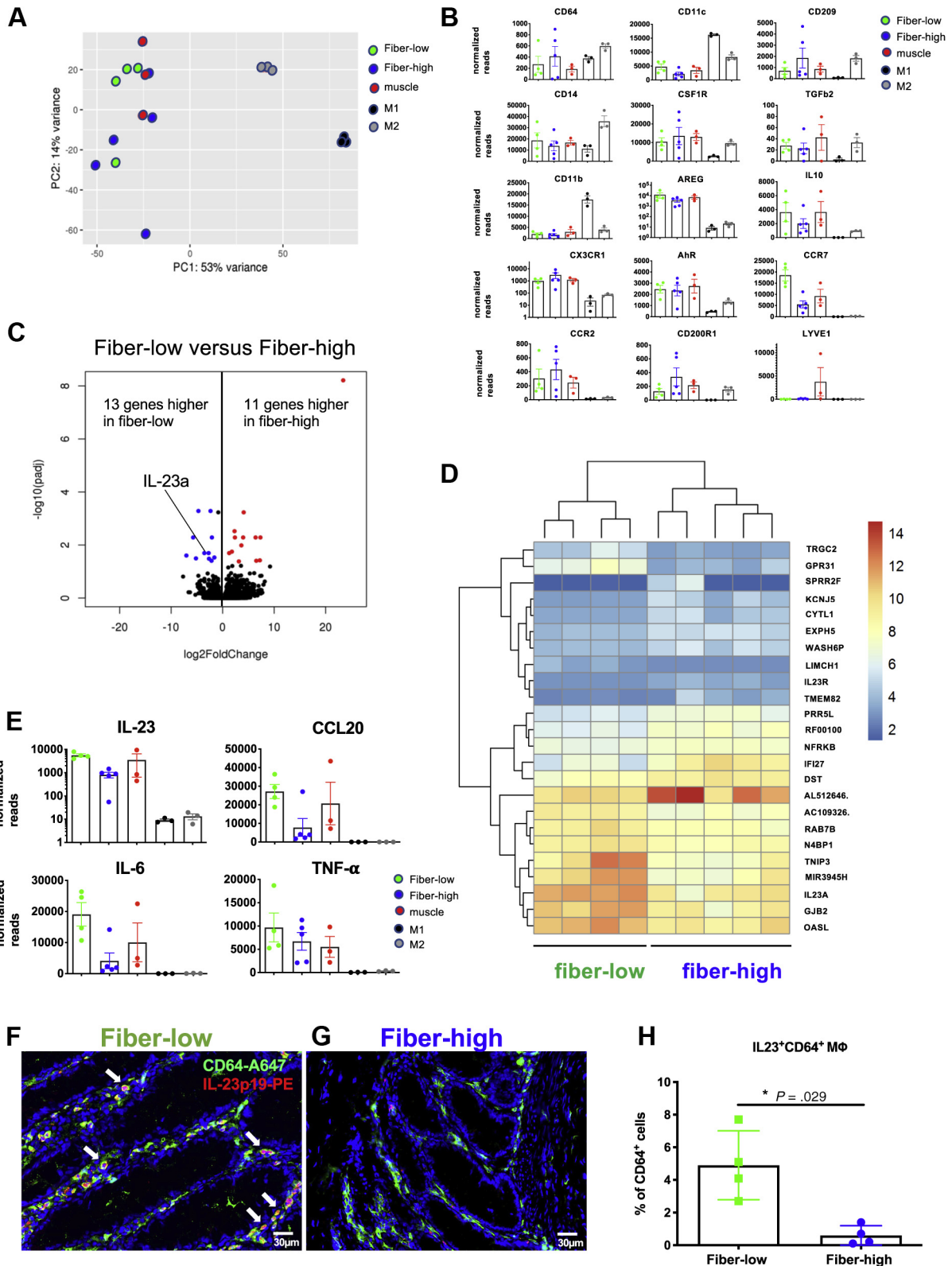
Figure 10. CD64⁺ LPM ϕ associate with neuronal AChE⁺ fibers in HSCR colon. (A) Immunofluorescence of epithelial/mucosal region from aganglionic and ganglionic colonic tissue from HSCR and control patients using CD64 (Alexa488, gray), AChE (Cy3, red), and tubulin (Alexa647, green). DAPI (blue) shows cell nuclei. Scale bar: 50 μ m. (B) Close-up view of images from (A). Scale bar: 10 μ m. Encircled areas mark the epithelial crypt/lumen. DC AG, aganglionic descending colon; DC G, ganglionic descending colon; DC control, ganglionic descending colon from control patients.

tissue from HSCR patients. Alpha diversity analysis showed comparable levels of operational taxonomic units (OTUs) as well as OTU richness (Shannon and Simpson index) (Figure 14A). Beta diversity analysis revealed intersample

relations (Figure 13D). On the phylum levels, Actinobacteria seemed to be less prevalent in aganglionic tissue compared with ganglionic tissue (Figure 14B). Within the bacterial family compositions, Actinobacteria were, by trend, less

prevalent in low-fiber segments compared with ganglionic DC, whereas other families were similarly expressed (Figure 14C). The main representative species of the

Actinobacteria were several *Bifidobacteria* (*B longum* (OTU1), *B bifidum* (OTU6), and *B pseudocatenulatum* (OTU5)), with *B longum* showing the highest frequency in all



samples (Table 3). Differential bacterial family analysis between low-fiber and high-fiber colonic tissue revealed a significant increase in Staphylococcaceae in low-fiber colonic segments, whereas in high-fiber tissue, Enterobacteriaceae and Clostridiales Family_XI were up-regulated (Figure 14D). Within the Staphylococcaceae family, *S aureus* (OTU7) was the only detectable species within the core microbiome (Table 3). The Clostridiales Family_XI was represented by 4 genera, ie, *Finegoldia* (OTU825), *Peptoniphilus* (OTU196), *Anaerococcus* (OTU543), and *Ezakiella* (OTU27, OTU63). The main representative species of Enterobacteriaceae family was *Escherichia coli* (OTU2), which represented the second most frequent bacterial species from the core microbiome (Table 3). These observations suggested a different composition of colon-associated bacteria between low-fiber and high-fiber tissue including a prevalence of Staphylococcaceae family in low-fiber segments lacking mucosal innervation. Because we only analyzed age-matched samples, the data analysis was limited by low sample numbers and high variance and thus needs further validation.

HSCR Patients With Low-Fiber Phenotype Showed a Higher Incidence of Postoperative Enterocolitis

Next, we evaluated the impact of fiber phenotype on the development of postoperative enterocolitis. One year after pull-through surgery, 42 HSCR patients were followed up, and postoperative enterocolitis manifestation was evaluated from medical records. Enterocolitis was defined to fulfill at least 3 of the following criteria: diarrhea (>3×/day), vomiting, temperature >38.5°C, antibiotics, hospitalization, abdominal distention, and high inflammatory blood parameters (ie, leukocytes, C-reactive protein). Anthropometric, clinical, environmental, maternal, and dietary factors, collected from the parent questionnaire, were analyzed for potential enterocolitis risk factors. A total of 9 of 42 patients developed postoperative enterocolitis within 1 year after surgery (Table 4). Development of enterocolitis was significantly associated with cesarean delivery at birth of the infant ($P = .012$). Seven of the 9 patients exhibited a low-fiber phenotype and only 2 a high-fiber phenotype,

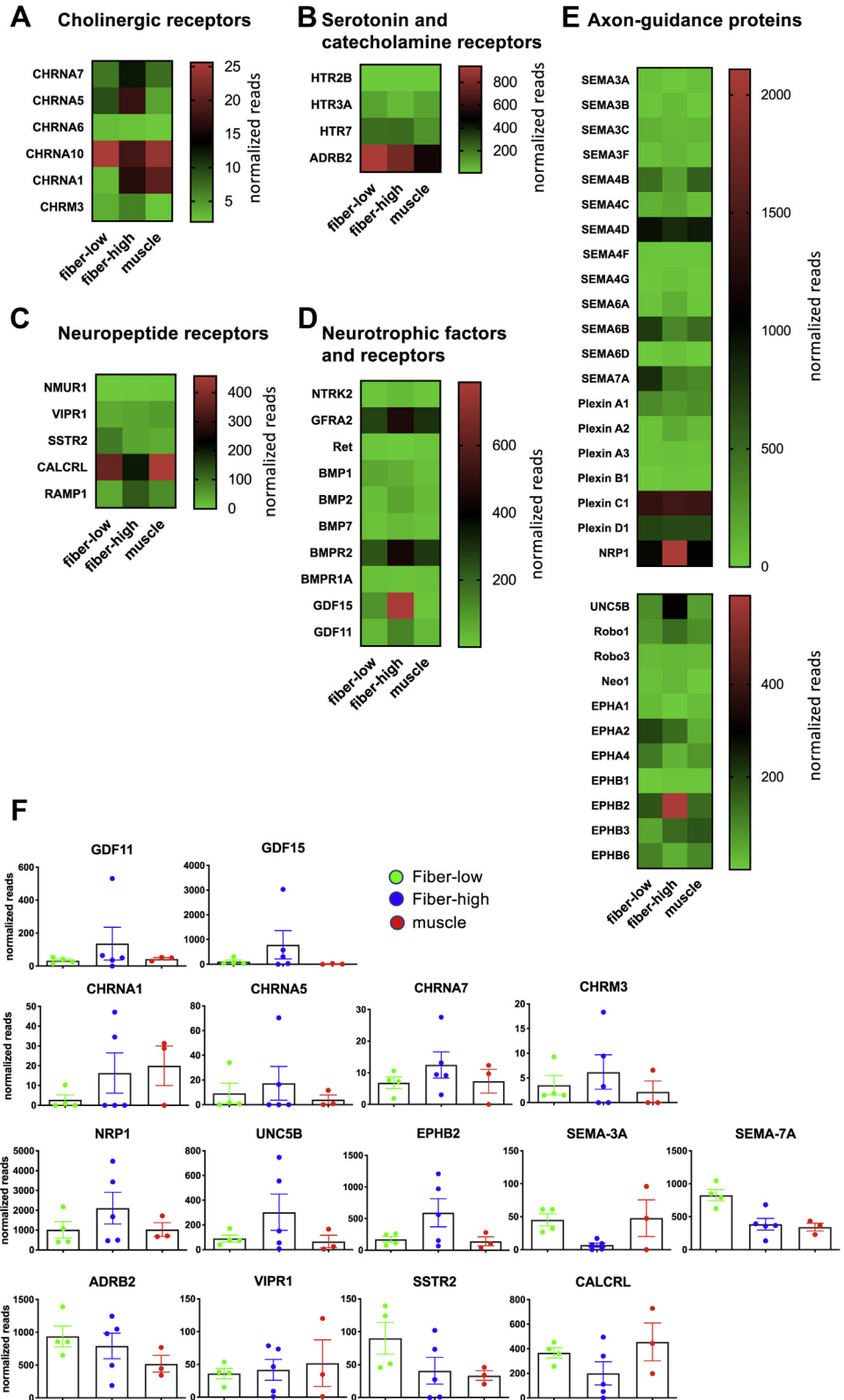
showing a higher incidence of low-fiber phenotype among the children who developed enterocolitis (78% versus 22%, $P = .634$). To validate the observations, we analyzed a retrospective HSCR patient cohort collected between 2003 and 2018 at the UKBB. A total of 29 HSCR patients were included. We did not observe any significant patient bias in terms of anthropometric or clinical factors between low-fiber and high-fiber tissues (Table 6). Enterocolitis development was recorded in 14 of 29 patients but showed no correlation with anthropometric or clinical data (Table 4). Strikingly, enterocolitis development correlated significantly with the fiber phenotype, showing a higher incidence in children with the low-fiber phenotype (86%, 12/14 children) compared with the high-fiber phenotype (14%, 2/14). These observations suggest that HSCR patients with low-fiber phenotype might have a higher risk of developing postoperative enterocolitis and that the fiber phenotype could serve as a predictive marker for development of prophylactic therapy.

Discussion

In recent years, multiple studies mainly using different mouse disease models have demonstrated the reciprocal relationship between the immune and nervous systems. However, in humans the difficulty of studying the individual effects of neurotransmitters leads to a lack of studies providing evidence of neuroimmune crosstalk. Here we suggested for the first time a correlation between the presence of colonic mucosal AChE⁺ nerve fiber innervation and a lower risk of developing enterocolitis in HSCR patients lacking an intrinsic ENS. Aganglionic DC samples showed elevated levels of inflammatory cytokines, which decreased in samples with a functional ENS (ganglionic DC) or in aganglionic high-fiber samples with mucosal AChE⁺ nerve fibers. Similar to aganglionic DC samples, the aganglionic low-fiber samples exhibited, by trend, elevated IL17, IL1 β , and IL6 cytokine levels. Th17 T cells in low-fiber samples were significantly elevated compared with high-fiber, aganglionic, and ganglionic DC samples. Strikingly, Th17 frequencies were not elevated in aganglionic DC samples, hypothesizing a different source of IL17 in those samples or that there might be regional

Figure 11. (See previous page). **M Φ isolated from fiber-high colonic tissue express diminished IL23 levels.** RNA sequencing was performed on sorted viable colonic M Φ and blood-derived M1 and M2 M Φ . (A) PCA plot shows similarity between the different populations based on their first 2 principal components. The top 500 genes, selected by highest row variance, were used. Fiber-low (green, n = 4); fiber-high (blue, n = 5); muscle (red, n = 3); M1 (black, n = 3); M2 (gray, n = 3). (B) Normalized sequence reads of selected macrophage-related genes. Scatter plots with bar show means \pm standard error of the mean. (C) Global transcriptional changes between macrophages isolated from fiber-low colonic tissue and fiber-high colonic tissue visualized by a volcano plot. Comparison of gene expression between the groups of samples was performed with the package DESeq2. The Wald test was used to generate P values and log₂ fold changes. Genes with an adjusted P value < .05 and log₂ fold change greater than 1 (red dots) and less than -1 (blue dots) were regarded as differentially expressed genes. (D) Heat map of differentially expressed genes. Each column represents 1 patient. (E) Normalized sequence reads of selected genes. Scatter plots with bar show means \pm standard error of the mean. (F and G) IL23⁺ CD64⁺ M Φ (arrows) were assessed by immunofluorescence in 5- μ m colonic cryosections. Representative images of mucosal/epithelial region from fiber-low tissue (F) and fiber-high tissue (G) are shown. Scale bar: 30 μ m. CD64 (A647, green); IL23p19-PE (red). (H) Quantitative analysis of IL23 expression in macrophages evaluated in images from 4 fiber-high and 4 fiber-low patients. Total of 900–4700 CD64⁺ cells per patient were analyzed for IL23 expression, and percentage of IL23⁺ CD64⁺ cells (% of total macrophages) was calculated. Scatter plots with bar show means \pm standard error of the means. Significance was determined using unpaired nonparametric Mann-Whitney test.

Figure 12. Receptors possibly involved in macrophage-neuron cross-talk. (A–E) Heat maps of selected genes possibly involved in macrophage-neuron crosstalk. Normalized reads are shown. RNA sequencing was performed on sorted viable colonic MΦ (CD45⁺ HLA⁺ CD64⁺) from mucosa of fiber-low (n = 4) and fiber-high (n = 5) colonic tissue as well as colonic muscle tissue (n = 3). Heat maps show mean values of each group. (A) Expression of nicotinic (CHRNA) and muscarinic (CHRM) ACh receptors. (B) Expression of serotonergic (HTR) and catecholaminergic (ADRB) receptors. (C) Expression of receptors for neuropeptide (NMUR1), VIP (VIPR1), somatostatin (SSTR2), and calcitonin gene-related peptide (CALCRL/RAMP1). (D) Expression of neurotrophins (BMP and GDF) and neurotrophin receptors (NTRK2 binds brain-derived neurotrophic factor [BDNF] and neurotrophin [NT]-4; GFRA2 and RET bind GDNF and neurturin). (E) Expression of axon-guidance proteins and respective receptors. SEMA bind to plexins or NRP1. UNC-5 represents the receptor for netrin. Receptor proteins ROBO1 and 3 bind slit proteins. Neogenin (Neo) receptor binds to repulsive guidance protein (RGM). Ephrins bind to Eph receptors EPHA and EPHB. (F) Normalized sequence reads of selected genes. Scatter plots with bar show means ± standard error of the mean.



compartmentalization of Th17 T cells.^{45,46} Furthermore, microbial colonization is crucial for Th17 T-cell differentiation and maintenance, explaining reduced Th17 levels in infants.^{47,48} The highest frequency of Treg cells was

detected in cholinergic high-fiber segments. Interestingly, Teratani et al⁴⁹ recently reported that activation of vagal parasympathetic nerves and enteric neurons stimulate mAChR⁺ colonic APCs to differentiate and maintain

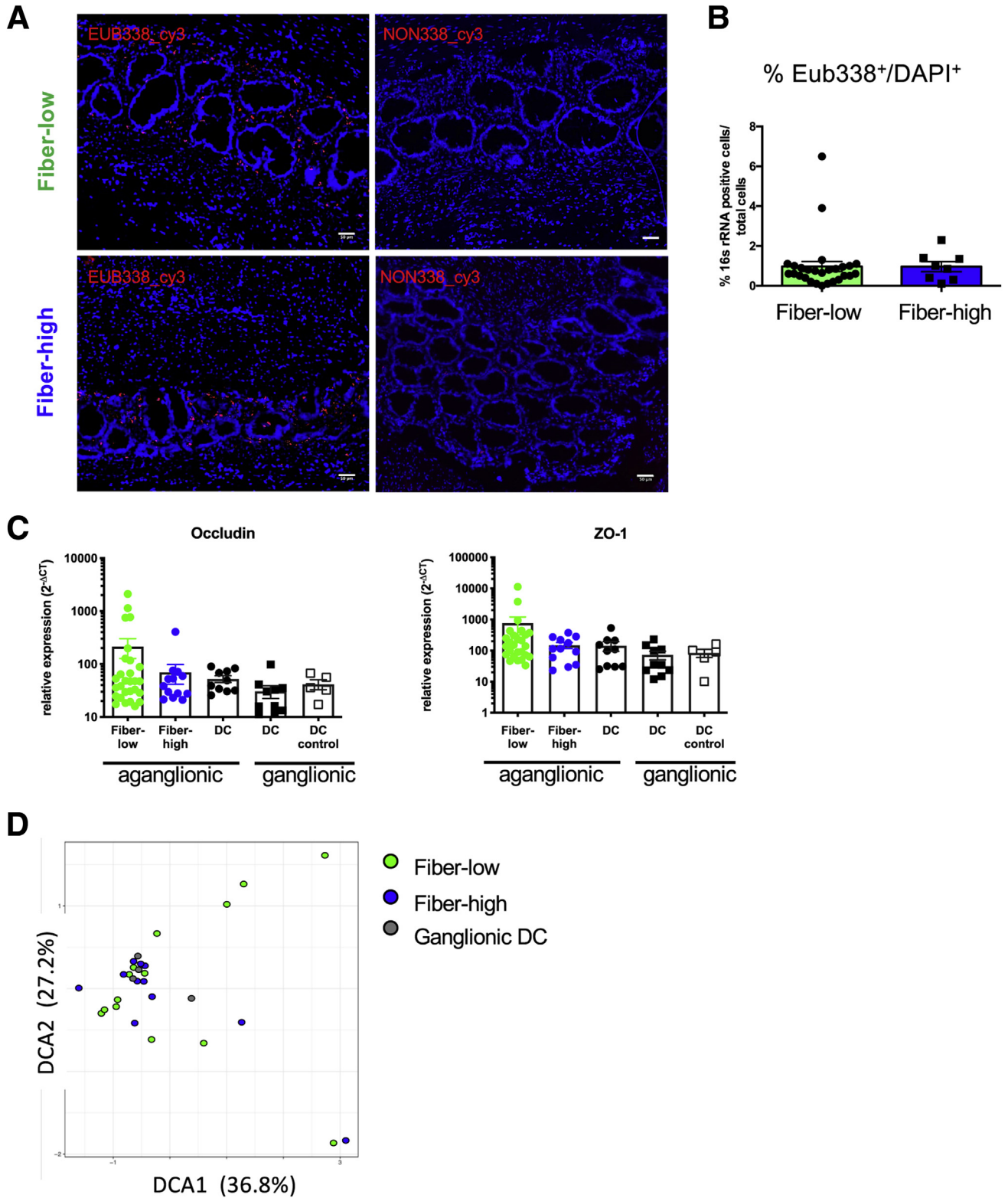


Figure 13. Microbial dysbiosis between fiber-low and fiber-high colonic tissue. (A and B) 16s rRNA FISH analysis was performed on 5- μ m cryosections of distal colon (rectum and sigmoid colon) of fiber-low (n = 27) and fiber-high (n = 8) HSCR patients using a bacteria-specific probe (EUB338). (A) Representative images of fiber-low and fiber-high colonic tissue probed with Cy3-labelled EUB338 and NON338 (negative control). Scale bar: 50 μ m. (B) Frequencies of translocated bacteria (16sRNA⁺/DAPI⁺) were determined using CellProfiler software and are shown as percentage of total DAPI⁺ cells. (C) qRT-PCR analysis of isolated colonic epithelial cells from different aganglionic (AG) and ganglionic (G) colonic segments of HSCR and control patients. Fiber-low (n = 28); fiber-high (n = 12); AG DC (n = 10); G DC (n = 10); control DC (n = 5). Occludin was not detectable in 2 fiber-low colonic tissue samples. (D) 16S rRNA analysis of colonic tissue from aganglionic (fiber-low, n = 14; fiber-high, n = 11) and ganglionic (DC, n = 4) segments of age-matched HSCR patients. Beta diversity 2-dimensional plot shows patterns of intersample relations using detrended correspondence analysis (DCA).

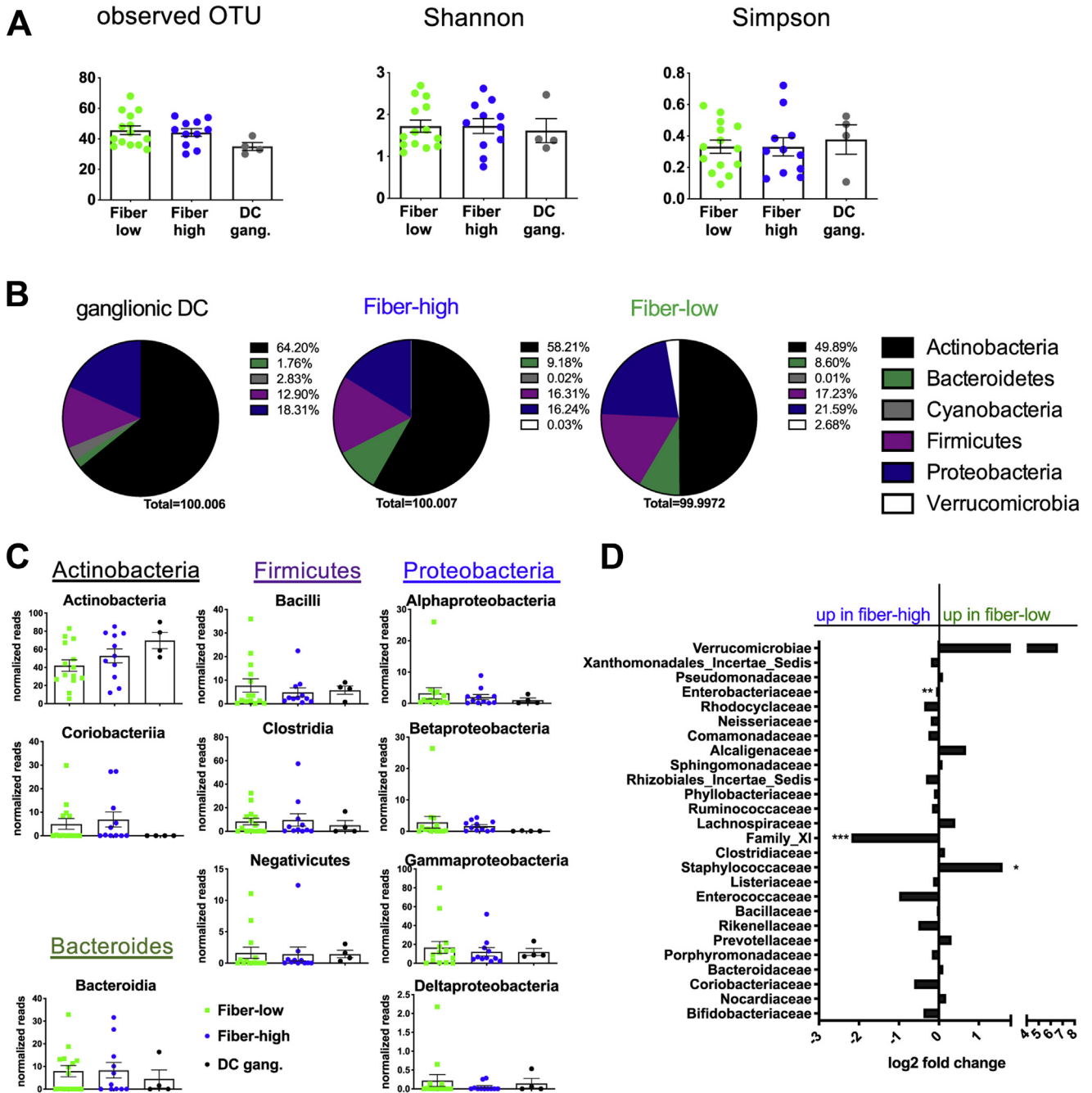


Figure 14. Colonic microbial dysbiosis in fiber-low colonic tissue from HSCR patients. (A–D) 16S rRNA analysis of colonic tissue from aganglionic (fiber-low, n = 14; fiber-high, n = 11) and ganglionic (DC ganglionic, n = 4) segments of age-matched HSCR patients. (A) Alpha diversity analysis shows effects on observed OTUs and estimated OTU richness by Shannon and Simpson indices. (B) Pie charts show microbial composition in each group on phylum level. (C) Normalized reads of bacterial classes dedicated to respective phyla. Scatter blots with bar show mean values ± standard error of the mean. Significance was determined using one-way analysis of variance multiple comparison analysis. (D) Differential bacterial family analysis of fiber-low versus fiber-high groups. Asterisks mark significantly changed families with adjusted P value <.05 (**P = 4.01 × 10⁻¹⁵; **P = 2.08 × 10⁻⁴; *P = 0.022). Families are assigned to respective phyla by color code.

colitis-protective colonic Treg cells in an aldehyde dehydrogenase-dependent manner.

Using confocal co-localization studies, we identified elongated tissue-resident MΦ in close proximity to AchE⁺ nerve fibers. Gabanyi et al³³ described bipolar-shaped MMΦ

with a tissue-protective anti-inflammatory M2 phenotype contrary to stellate-shaped LPMΦ. The elongated profile allows MMΦ to interact and wrap around neighboring neurites. At steady state, MMΦ regulate ENS functions and therefore gut motility by providing bone morphogenetic

Table 3. Core Microbiome of 16S rDNA Sequencing of Colonic Tissue

OTU	Sample	Size	Freq	DomOTU	Dom	size	DomID	Min	LoQ	Med	HiQ	Max	Taxonomy
1	36	748468	0.339	—	—	—	11	637	13721	36291	84291		k:Bacteria,p:Actinobacteria,c:Actinobacteria,o:Bifidobacteriales,f:Bifidobacteriaceae,g:Bifidobacterium,s:Bifidobacterium_longum_E18
2	36	187671	0.0851	—	—	—	3	477	2619	7769	26234		k:Bacteria,p:Proteobacteria,c:Gammaproteobacteria,o:Enterobacteriales,f:Enterobacteriaceae,g:Escherichia-Shigella,s:Escherichia_coli_KOEGE_62_[175a]
4	36	48058	0.0218	—	—	—	5	33	219	847	21388		k:Bacteria,p:Proteobacteria,c:Gammaproteobacteria
10	36	48045	0.0218	—	—	—	1	150	423	2473	8624		k:Bacteria,p:Firmicutes,c:Bacilli,o:Lactobacillales,f:Enterococcaceae,g:Enterococcus,s:Enterococcus_faecalis_EnGen0246
7	36	38523	0.0175	—	—	—	22	77	132	297	23544		k:Bacteria,p:Firmicutes,c:Bacilli,o:Bacillales,f:Staphylococcaceae,g:Staphylococcus,s:Staphylococcus_aureus_M1256
21	36	29874	0.0135	—	—	—	18	94	178	530	9954		k:Bacteria,p:Actinobacteria,c:Actinobacteria,o:Corynebacteriales,f:Corynebacteriaceae
42	36	21712	0.00984	—	—	—	28	116	316	668	2844		k:Bacteria,p:Proteobacteria,c:Alphaproteobacteria,o:Rhizobiales,f:Rhizobiales_Incertae_Sedis,g:Phreatobacter
53	36	2804	0.00127	—	—	—	1	15	36	70	465		k:Bacteria,p:Proteobacteria,c:Betaproteobacteria,o:Burkholderiales,f:Comamonadaceae,g:Delftia
43	36	2639	0.0012	—	—	—	3	12	29	68	501		k:Bacteria,p:Firmicutes,c:Bacilli,o:Bacillales,f:Bacillaceae,g:Anaerobacillus
17	35	39122	0.0177	—	—	—	24	106	264	668	7842		k:Bacteria,p:Proteobacteria,c:Alphaproteobacteria,o:Rhizobiales,f:Phyllobacteriaceae,g:Phyllobacterium
6	34	83714	0.0379	—	—	—	1	12	349	3129	26184		k:Bacteria,p:Actinobacteria,c:Actinobacteria,o:Bifidobacteriales,f:Bifidobacteriaceae,g:Bifidobacterium,s:Bifidobacterium_bifidum_ATCC_29521_=_JCM_1255_=_DSM_20456
19	34	7827	0.00355	—	—	—	1	8	36	132	1980		k:Bacteria,p:Firmicutes,c:Bacilli,o:Bacillales,f:Bacillaceae,g:Bacillus,s:Bacillus_subtilis_subsp._subtilis
29	34	5688	0.00258	—	—	—	1	13	47	108	1491		k:Bacteria,p:Firmicutes,c:Bacilli,o:Bacillales,f>Listeriaceae,g>Listeria,s>Listeria_monocytogenes
26	33	11261	0.0051	—	—	—	1	11	48	257	2658		k:Bacteria,p:Proteobacteria,c:Gammaproteobacteria,o:Pseudomonadales,f:Pseudomonadaceae,g:Pseudomonas,s:Pseudomonas_aeruginosa_PACS2
35	33	5295	0.0024	—	—	—	1	8	41	129	1018		k:Bacteria,p:Firmicutes,c:Bacilli,o:Lactobacillales,f:Lactobacillaceae,g:Lactobacillus,s:Lactobacillus_fermentum
65	33	5228	0.00237	—	—	—	2	18	56	136	1566		k:Bacteria,p:Proteobacteria,c:Gammaproteobacteria,o:Xanthomonadales,f:Xanthomonadales_Incertae_Sedis,g:Acidibacter
12	32	20721	0.00939	—	—	—	1	1	5	291	5809		k:Bacteria,p:Bacteroidetes,c:Bacteroidia,o:Bacteroidales,f:Bacteroidaceae,g:Bacteroides
5	31	40841	0.0185	—	—	—	1	3	21	100	20809		k:Bacteria,p:Actinobacteria,c:Actinobacteria,o:Bifidobacteriales,f:Bifidobacteriaceae,g:Bifidobacterium,s:Bifidobacterium_pseudocatenulatum_DSM_20438_=_JCM_1200_=_LMG_10505
50	31	7624	0.00346	—	—	—	1	1	7	63	2538		k:Bacteria,p:Actinobacteria,c:Actinobacteria,o:Bifidobacteriales,f:Bifidobacteriaceae,g:Bifidobacterium

Table 3. Continued

OTU	Sample	Size	Freq	DomOTU	Dom size	DomID	Min	LoQ	Med	HiQ	Max	Taxonomy
831	30	21177	0.0096	—	—	—	1	3	34	303	13401	k:Bacteria,p:Firmicutes,c:Negativicutes,o:Selenomonadales,f:Veillonellaceae,g:Veillonella
8	29	23263	0.0105	—	—	—	1	2	21	83	20960	k:Bacteria,p:Proteobacteria,c:Gammaproteobacteria,o:Enterobacteriales,f:Enterobacteriaceae
812	28	12449	0.00564	—	—	—	1	7	29	68	5886	k:Bacteria,p:Firmicutes,c:Clostridia,o:Clostridiales,f:Family_XI,g:Finegoldia
3	27	60864	0.0276	—	—	—	1	2	6	1975	26467	k:Bacteria,p:Bacteroidetes,c:Bacteroidia,o:Bacteroidales,f:Bacteroidaceae,g:Bacteroides
75	27	4646	0.00211	—	—	—	2	10	36	112	2356	k:Bacteria,p:Proteobacteria,c:Alphaproteobacteria,o:Sphingomonadales,f:Sphingomonadaceae,g:Sphingomonas
361	26	9680	0.00439	—	—	—	10	20	70	170	2600	k:Bacteria,p:Firmicutes,c:Bacilli,o:Lactobacillales,f:Enterococcaceae,g:Enterococcus
69	26	3322	0.00151	—	—	—	1	5	15	56	2100	k:Bacteria,p:Proteobacteria,c:Betaproteobacteria,o:Burkholderiales,f:Comamonadaceae,g:Acidovorax
44	25	12070	0.00547	—	—	—	1	3	23	496	4016	k:Bacteria,p:Actinobacteria,c:Actinobacteria,o:Bifidobacteriales,f:Bifidobacteriaceae,g:Bifidobacterium
32	25	9946	0.00451	—	—	—	1	2	10	98	4090	k:Bacteria,p:Firmicutes,c:Bacilli,o:Lactobacillales,f:Enterococcaceae,g:Enterococcus,s:Enterococcus_pallens_ATCC_BAA-351
9	24	93012	0.0422	—	—	—	2	6	88	4570	36070	k:Bacteria,p:Actinobacteria,c:Coriobacteriia,o:Coriobacteriales,f:Coriobacteriaceae,g:Collinsella,s:Collinsella_aerofaciens
196	24	6264	0.00284	—	—	—	1	6	12	172	2096	k:Bacteria,p:Firmicutes,c:Clostridia,o:Clostridiales,f:Family_XI,g:Peptoniphilus
541	22	40265	0.0183	—	—	—	1	2	9	318	16032	k:Bacteria,p:Firmicutes,c:Clostridia,o:Clostridiales,f:Family_XI,g:Anaerococcus
22	22	21390	0.0097	—	—	—	1	8	157	507	13925	k:Bacteria,p:Actinobacteria,c:Actinobacteria,o:Actinomycetales,f:Actinomycetaceae,g:Varibaculum
13	21	40558	0.0184	—	—	—	1	7	55	1183	27312	k:Bacteria,p:Proteobacteria,c:Betaproteobacteria,o:Burkholderiales,f:Alcaligenaceae,g:Sutterella
14	21	19704	0.00893	—	—	—	1	3	6	30	11191	k:Bacteria,p:Bacteroidetes,c:Bacteroidia,o:Bacteroidales,f:Bacteroidaceae,g:Bacteroides
24	21	5238	0.00237	—	—	—	1	6	22	320	1720	k:Bacteria,p:Firmicutes,c:Clostridia,o:Clostridiales,f:Clostridiaceae_1,g:Clostridium_sensu_stricto_1,s:Clostridium_paraputrificum
41	20	13038	0.00591	—	—	—	2	4	28	1340	3766	k:Bacteria,p:Firmicutes,c:Clostridia,o:Clostridiales,f:Ruminococcaceae,g:Flavonifractor
20	19	15971	0.00724	—	—	—	1	2	7	202	9414	k:Bacteria,p:Bacteroidetes,c:Bacteroidia,o:Bacteroidales,f:Bacteroidaceae,g:Bacteroides
23	19	8516	0.00386	—	—	—	1	1	3	78	5426	k:Bacteria,p:Bacteroidetes,c:Bacteroidia,o:Bacteroidales,f:Bacteroidaceae,g:Bacteroides
82	19	3336	0.00151	—	—	—	4	10	28	100	1362	k:Bacteria,p:Proteobacteria,c:Betaproteobacteria,o:Rhodocyclales,f:Rhodocyclaceae,g:Methyloversatilis,s:Methyloversatilis_universalis_EHg5

Table 3. Continued

OTU	Sample	Size	Freq	DomOTU	Dom	size	DomID	Min	LoQ	Med	HiQ	Max	Taxonomy
16	17	47772	0.0217	—	—	—	2	2	6	26	23950	k:Bacteria,p:Actinobacteria,c:Actinobacteria,o:Actinomycetales,f:Actinomycetaceae,g:Actinomyces,s:Actinomyces_turicensis_ACS-279-V-Col4	
55	17	2996	0.00136	—	—	—	1	1	2	31	1278	k:Bacteria,p:Firmicutes,c:Bacilli,o:Lactobacillales,f:Lactobacillaceae,g:Lactobacillus,s:Lactobacillus_casei_5b	
11	16	78452	0.0356	—	—	—	2	8	24	164	77484	k:Bacteria,p:Actinobacteria,c:Actinobacteria,o:Actinomycetales,f:Actinomycetaceae,g:Actinomyces,s:Actinomyces_europaeus_ACS-120-V-Col10b	
34	16	15444	0.007	—	—	—	2	6	88	1078	10006	k:Bacteria,p:Actinobacteria,c:Actinobacteria,o:Actinomycetales,f:Actinomycetaceae,g:Actinomyces	
18	16	13394	0.00607	—	—	—	1	1	5	34	13099	k:Bacteria,p:Bacteroidetes,c:Bacteroidia,o:Bacteroidales,f:Bacteroidaceae,g:Bacteroides	
38	16	4860	0.0022	—	—	—	1	2	8	33	4592	k:Bacteria,p:Cyanobacteria,c:Chloroplast	
30	15	17280	0.00783	—	—	—	2	2	18	334	7174	k:Bacteria,p:Bacteroidetes,c:Bacteroidia,o:Bacteroidales,f:Rikenellaceae,g:Alistipes,s:Alistipes_sp_AL-1	
31	15	5940	0.00269	—	—	—	1	1	25	159	3221	k:Bacteria,p:Firmicutes,c:Clostridia,o:Clostridiales,f:Lachnospiraceae,g:Lachnoclostridium	
56	15	2690	0.00122	—	—	—	1	2	46	150	1418	k:Bacteria,p:Firmicutes,c:Clostridia,o:Clostridiales,f:Lachnospiraceae,g:Blautia	
869	14	18179	0.00824	—	—	—	1	2	45	1432	11357	k:Bacteria,p:Firmicutes,c:Negativicutes,o:Selenomonadales,f:Veillonellaceae,g:Veillonella,s:Veillonella_sp_FFA-2014	
25	13	47392	0.0215	—	—	—	4	4	12	384	38992	k:Bacteria,p:Actinobacteria,c:Coriobacteriia,o:Coriobacteriales,f:Coriobacteriaceae,g:Atopobium,s:Atopobium_minutum_10063974	
36	13	13810	0.00626	—	—	—	2	4	42	118	5966	k:Bacteria,p:Bacteroidetes,c:Bacteroidia,o:Bacteroidales,f:Porphyromonadaceae,g:Parabacteroides	
51	13	4162	0.00189	—	—	—	1	5	48	308	2476	k:Bacteria,p:Proteobacteria,c:Deltaproteobacteria,o:Desulfovibrionales,f:Desulfovibrionaceae,g:Bilophila,s:Bilophila_wadsworthia_3_1_6	
47	13	3704	0.00168	—	—	—	1	2	3	162	3021	k:Bacteria,p:Firmicutes,c:Clostridia,o:Clostridiales,f:Lachnospiraceae,g:Blautia	
49	13	3246	0.00147	—	—	—	1	1	12	94	2146	k:Bacteria,p:Firmicutes,c:Clostridia,o:Clostridiales,f:Lachnospiraceae,g:Fusicatenibacter	
39	13	2864	0.0013	—	—	—	1	11	53	372	1164	k:Bacteria,p:Firmicutes,c:Clostridia,o:Clostridiales,f:Clostridiaceae_1,g:Clostridium_sensu_stricto_1,s:Clostridium_perfringens_C_str_JGS1495	
54	13	2692	0.00122	—	—	—	1	2	95	135	952	k:Bacteria,p:Bacteroidetes,c:Bacteroidia,o:Bacteroidales,f:Bacteroidaceae,g:Bacteroides	
15	12	31270	0.0142	—	—	—	3	4	16	59	30279	k:Bacteria,p:Verrucomicrobia,c:Verrucomicrobiae,o:Verrucomicrobiales,f:Verrucomicrobiaceae,g:Akkermansia	
37	11	5809	0.00263	—	—	—	1	1	2	897	3587	k:Bacteria,p:Firmicutes,c:Bacilli,o:Lactobacillales,f:Lactobacillaceae,g:Lactobacillus,s:Lactobacillus_rhamnosus_DSM_20021=_JCM_1136=_NBRC_3425	
28	10	15240	0.00691	—	—	—	1	5	637	1952	9648	k:Bacteria,p:Firmicutes,c:Clostridia,o:Clostridiales,f:Ruminococcaceae	

Table 3. Continued

OTU	Sample	Size	Freq	DomOTU	Dom size	DomID	Min LoQ	Med	HiQ	Max	Taxonomy	
48	10	6673	0.00302	—	—	—	1	3	5	207	3953	k:Bacteria,p:Actinobacteria,c:Actinobacteria,o:Actinomycetales,f:Actinomycetaceae,g:Actinobaculum,s:Actinobaculum_massiliae_ACS-171-V-Col2
68	10	3685	0.00167	—	—	—	1	1	215	761	1500	k:Bacteria,p:Firmicutes,c:Clostridia,o:Clostridiales,f:Ruminococcaceae,g:Faecalibacterium
925	9	8666	0.00393	—	—	—	1	2	10	95	5933	k:Bacteria,p:Firmicutes,c:Clostridia,o:Clostridiales,f:Ruminococcaceae,g:Anaerotruncus,s:Clostridiales_bacterium_VE202-13
40	9	3327	0.00151	—	—	—	1	1	2	3	3079	k:Bacteria,p:Proteobacteria,c:Betaproteobacteria,o:Burkholderiales,f:Alcaligenaceae,g:Sutterella
62	9	2509	0.00114	—	—	—	1	1	1	37	1398	k:Bacteria,p:Firmicutes,c:Clostridia,o:Clostridiales,f:Lachnospiraceae,g:Roseburia
52	8	7846	0.00356	—	—	—	2	38	124	1712	5452	k:Bacteria,p:Firmicutes,c:Clostridia,o:Clostridiales,f:Ruminococcaceae,g:Faecalibacterium
33	8	5962	0.0027	—	—	—	1	4	70	208	5591	k:Bacteria,p:Firmicutes,c:Clostridia,o:Clostridiales,f:Lachnospiraceae,g:Blautia
45	8	3781	0.00171	—	—	—	1	1	6	445	2946	k:Bacteria,p:Firmicutes,c:Clostridia,o:Clostridiales,f:Lachnospiraceae,g:Lachnoclostridium
60	8	3273	0.00148	—	—	—	1	1	132	1346	1581	k:Bacteria,p:Proteobacteria,c:Betaproteobacteria,o:Neisseriales,f:Neisseriaceae,g:Eikenella
27	7	14998	0.0068	—	—	—	3	3	17	481	14392	k:Bacteria,p:Firmicutes,c:Clostridia,o:Clostridiales,f:Family_XI,g:Ezakiella
57	7	6330	0.00287	—	—	—	2	4	6	88	6174	k:Bacteria,p:Bacteroidetes,c:Bacteroidia,o:Bacteroidales,f:Prevotellaceae,g:Prevotella
70	7	3574	0.00162	—	—	—	1	3	35	275	3217	k:Bacteria,p:Firmicutes,c:Clostridia,o:Clostridiales,f:Ruminococcaceae,g:Subdoligranulum
101	7	2778	0.00126	—	—	—	2	2	18	958	1250	k:Bacteria,p:Firmicutes,c:Clostridia,o:Clostridiales,f:Ruminococcaceae,g:Faecalibacterium
77	6	3612	0.00164	—	—	—	2	30	46	1616	1884	k:Bacteria,p:Firmicutes,c:Clostridia,o:Clostridiales,f:Ruminococcaceae,g:Ruminococcaceae_UCG-005
46	6	2824	0.00128	—	—	—	1	1	74	172	2574	k:Bacteria,p:Bacteroidetes,c:Bacteroidia,o:Bacteroidales,f:Porphyromonadaceae,g:Parabacteroides
63	5	4055	0.00184	—	—	—	1	3	300	387	3364	k:Bacteria,p:Firmicutes,c:Clostridia,o:Clostridiales,f:Family_XI,g:Ezakiella
100	5	2420	0.0011	—	—	—	8	38	136	156	2082	k:Bacteria,p:Actinobacteria,c:Coriobacteriia,o:Coriobacteriales,f:Coriobacteriaceae,g:Slackia
87	4	2856	0.00129	—	—	—	2	32	950	1872	1872	k:Bacteria,p:Firmicutes,c:Clostridia,o:Clostridiales,f:Lachnospiraceae,g:[Eubacterium]_hallii_group

Table 4. Risk Factors for Postoperative Enterocolitis Development

Prospective HSCR patient cohort	No. patients positive for risk factor/ available patient data (percentage)	Enterocolitis		
		Yes, n = 9	No, n = 33	P value
Anthropometric data and potential risk factors (no. of available patient data)				
	Total patients followed up, n = 42			
Age at operation, mo (42)	5 [1–127]	3 [1–127]	5 [2–70]	.211
Sex, male (42)	34/42 (81%)	7 (78%)	27 (81%)	.784
Preterm birth (38)	3/38 (7%)	2 (22%)	1 (3%)	.068
Operative procedure transanal (42)	37/42 (88%)	8 (89%)	29 (88%)	.934
Length of aganglionosis (42)	2 [1–5]	1 [1–5]	2 [1–5]	.061
Pets (37)	12/37 (32%)	1 (11%)	11 (39%)	.116
Patient living in rural area (40)	20/40 (50%)	3 (33%)	17 (55%)	.256
Antibiotic treatment (38)	5/38 (13%)	2 (22%)	3 (10%)	.357
Siblings (39)	30/39 (77%)	8 (89%)	22 (73%)	.331
Breastfed at operation (39)	36/39 (92%)	9 (100%)	27 (90%)	.323
Maternal age at delivery, y (35)	28 [21–43]	27 [23–39]	29 [21–43]	.788
Parental smoking (38)	9/38 (21%)	4 (44%)	5 (17%)	.094
Cesarean section (38)	14/38 (37%)	6 (75%)	8 (27%)	.012
Maternal allergy (38)	10/38 (26%)	1 (11%)	9 (31%)	.236
Fiber-low (42)	30/42 (71%)	7 (78%)	23 (70%)	.634
Retrospective HSCR patient cohort (no. of available patient data)				
	Total, n = 29	Yes, n = 14	No, n = 15	P value
Age at operation (mo) (29)	5 [1–171]	4 [1–48]	9 [1–171]	.229
Sex, male (29)	25/29 (86%)	11 (79%)	14 (93%)	.249
Preterm birth (29)	2/29 (7%)	1 (7%)	1 (7%)	.960
Antibiotic treatment (29)	21/29 (72%)	10 (7%)	11 (73%)	.909
Cesarean section (29)	12/29 (41%)	7 (50%)	5 (33%)	.124
Fiber-low (29)	15/29 (52%)	12 (86%)	3 (20%)	<.001

NOTE. Values are median [range] or number of patients (percentage %).

protein (BMP) 2 in response to microbial stimuli.³² Tamoxifen-induced deletion of CX3CR1⁺ tissue-resident MΦ leads to loss of enteric neurons.⁵⁰ Interestingly, MMΦ develop independently of the ENS.⁵¹ Neuroimmune modulation seems to involve different neuronal receptors. Upon *Salmonella typhimurium* infection, MMΦ interact with sympathetic adrenergic neurons via β2 adrenergic receptors to induce a tissue- and neuron-protective gene expression program.³³ In a model of POI that is characterized by a surgery-induced inflammatory response of MMΦ and impaired motility, VN stimulation or pharmacologic triggering of cholinergic enteric neurons prevented MΦ activation and reduced POI in an α7nAChR-dependent manner in both mice and humans.³⁹ In a murine model of food allergy, VN stimulation ameliorated disease severity independently of α7nAChR.⁵² Uptake of food antigens by anti-inflammatory CX3CR1⁺ MΦ and subsequent induction of food-specific Tregs effectively prevent allergic reactions.²⁹ VN stimulation increases phagocytic activity in CX3CR1⁺ MΦ independently of α7nAChR, but phagocytic activity remains dependent on α4β2nAChR.⁵³ Using a murine helminth infection model, it has been demonstrated that the neuropeptide neuromedin U activates ILC2, thus increasing the protective immune response and parasitic clearance.^{40,41} In contrast, signals from sympathetic adrenergic neurons lead to attenuated ILC2 effector function and prevent chronic pathologic type 2 inflammation via activation

of ILC2-specific β2 adrenergic receptors.⁵⁴ In the current study we performed transcriptional analysis of sorted MΦ isolated from high-fiber and low-fiber colonic tissue. Although the analysis did not provide a functional relationship between MΦ and cholinergic fibers, we found a tendency of elevated nicotinic and muscarinic receptors expressed by MΦ isolated from high-fiber compared with low-fiber tissue. Colonic MΦ represent the main APC subset in the colon, and their phenotype and secreted cytokines influence CD4 T-helper cell differentiation.^{28–30,55} However, a functional mechanism between the different patient-derived colonic macrophages and the observed T-helper cell subsets still has to be provided. The results obtained from experiments using blood-derived M1 and M2 MΦ cannot be extrapolated to the colonic population and only exemplify the impact of MΦ phenotype on T-helper cell differentiation.

In our study, IL23, a cytokine promoting the maintenance of Th17 cells, is significantly increased in LPMΦ isolated from low-fiber tissue compared with LPMΦ isolated from innervated high-fiber tissue. Genome-wide studies identified genes, including the gene for IL23 receptor, associated with a susceptibility to inflammatory bowel disease.⁵⁶ IL23 is produced by dendritic cells and MΦ in response to extracellular bacteria and fungi recognized by special innate pattern-recognition receptors: the toll-like receptor 2 and nucleotide oligomerization domain

Table 5. Overview of Retrospective HSCR Patient Cohort

Study Number	Sex	Age at Surgery (months)	OP technique: Del la Torre (1); Soave transanal (2); Soave transabdominal (3); Swenson transanal (4); Svenson transabdominal (5); Duhamel (6); Rehbein (7)	Length of AG	Fiber score	Postoperative clinical symptoms: Constipation (1); Incontinence (2); Enterocolitis (3); Pain (4); Impaired growth (5); Stenose/ileus (6)	Postoperative clinical treatment: Laxative (1); Clyster (2); Botox (3); Antibiotics (4); Colonic irrigation (5); Pre-/probiotics (6)
1	F	22	2	L-HSCR	low	3, 6	4,5,6
2	F	7	6	TCA	low	1,3,5,6	2,4
3	M	2	1	S-HSCR	high	1	3,5,6
4	M	171	1	TCA	low	no	no
5	M	9.5	1	TCA	high	1	6
6	M	2	1	L-HSCR	low	3, 6	3,4,5,6
7	M	3.5	1	S-HSCR	high	1, 2	2
8	M	1	1	S-HSCR	high	no	no
9	M	10.7	1	S-HSCR	high	1,6	5
10	F	25	2	S-HSCR	high	no	no
11	M	48	1	S-HSCR	high	1,3,6	1,2,3,4,5
12	M	52	2	S-HSCR	high	2	1,5,6
13	M	1	1	L-HSCR	low	1,2,3	2,4,5
14	M	28.5	1	S-HSCR	high	2	6
15	M	4	7	TCA	low	1,3,4,5,6	4,5,6
16	F	2.8	1	TCA	low	3	4,5
17	M	3.7	1	S-HSCR	low	3	no
18	M	8	6	S-HSCR	low	1,3	1,5
19	M	5	1	L-HSCR	high	2	no
20	M	7	1	S-HSCR	high	3	4
21	M	9	1	TCA	low	3,5	3,4,5
22	M	60	2	S-HSCR	high	no	no
23	M	67	1	L-HSCR	high	2,6	6
25	M	1.5	1	S-HSCR	low	3	1,2,3,4,5
27	M	3.5	1	S-HSCR	low	no	no
30	M	3	1	L-HSCR	low	1,3	3,4,5,6
31	M	4.3	1	S-HSCR	low	3,6	5
32	M	1.5	1	S-HSCR	low	no	no
33	M	2	1	L-HSCR	high	5	no

Length of aganglionosis: TCA (total colonic aganglionosis); L-HSCR (long-segmented HSCR); S-HSCR (short-segmented HSCR).

Table 6. Characteristics of HSCR Retrospective Patient Cohort

Anthropometric data and potential risk factors	No. patients positive for risk factor/ total patients (%)	Fiber-low (n = 15)	Fiber-high (n = 14)	P value
Age at operation, mo	5 [1–171]	3 [1–127]	9.5 [1–67]	.063
Sex, male	25/29 (86)	12 (80)	13 (93)	.316
Preterm birth	2/29 (7)	1 (7)	1 (7)	.960
Antibiotic treatment	21/29 (72)	12 (80)	9 (64)	.550
Caesarean section	12/29 (41)	6 (40)	6 (43)	.876

NOTE. Values are median [range] or number (percentage).

containing protein 2. Under inflammatory conditions, monocyte-derived CCR2⁺ CX3CR1⁺ M Φ infiltrate the gut mucosa and prime Th17 cell responses. At steady state, CX3CR1⁺ M Φ are indispensable for epithelial integrity, control of bacterial translocation, and development of oral and commensal tolerance by secreting anti-inflammatory cytokines and maintaining Treg.²⁹

In our study, we found higher tissue expression of CX3CR1 than CCR2 in high-fiber colonic segments of HSCR patients and described 2 M Φ populations based on CD14 expression and shape. CD14⁺ bipolar M Φ were found in close proximity to nerve fibers in both muscularis and lamina propria, expressing low levels of CCR7, suggesting a tissue-resident phenotype. CD14^{low} stellate-shaped M Φ were present in non-innervated LP from low-fiber tissue, expressing high levels of CCR7, thus indicating a migratory population. On the basis of their transcriptional profile, LPM Φ isolated from both low-fiber and high-fiber colonic tissues exhibited a gut-imprinted M2 phenotype (CX3CR1, AREG, AhR, CSF1R, CD200R, CD209, TGF β 2, and IL10), but they differed in Th17 cytokines (IL23 and IL6) and Th17 chemokines (CCL20). Consequently, the presence of mucosal AChE⁺ nerve fibers seemed to be associated with reduced type-17 immune responses. In a murine model of psoriasis, sensory nociceptive neurons augment dermal dendritic cell-mediated IL23 production.⁴² The neurons directly sense disease-inducing *Candida albicans* and release the neuropeptide calcitonin gene-related peptide, which increases IL23 production.⁴³ Surprisingly, another study uncovered an immunosuppressive effect of nociceptive fibers during *S aureus* infection, indicating a role for the properties of the underlying pathogen or target immune cell on neuronal-induced immune modulation.⁵⁷

Neurotrophic factors and their respective receptors are crucial for ENS development and function. In fact, the underlying genetic defects in HSCR patients involve signaling pathways controlling migration and development of the ENS, including the 2 major HSCR genes, rearranged during transfection (Ret) and endothelin receptor type B (EndrB). In a study using Ret-deficient mice, the authors demonstrated that microbiota-induced glial cell-derived neurotrophic factors induce IL22 in Ret-expressing ILC3, therefore maintaining intestinal homeostasis.⁵⁸ Ret expression was not detected in colonic M Φ populations, and we did not detect any changes in ILC3 frequencies between low-fiber and high-fiber colonic segments. Here we used RNA-seq transcriptional analysis of sorted colonic M Φ to identify factors and receptors possibly involved in neuro-immune interactions. However, the RNA-seq data were highly variable within the groups, and a proof of a functional relationship is missing. Further studies are needed to fully uncover mechanisms involved in neuron-M Φ interactions. Besides the potential contribution of nicotinic and muscarinic receptors, we considered the contribution of neurotrophic factors, axon-guidance proteins, and their respective receptors in possible neuron-M Φ interactions. GDF15 has been reported to suppress inflammatory responses in a murine model of endotoxin-induced sepsis and prevent maturation of inflammatory dendritic cells in a heart

transplantation model.⁵⁹ Using an imiquimod- or IL23-induced mouse model of psoriasis-like skin inflammation, GDF11 administration attenuated the severity of skin inflammation via suppression of the nuclear factor kappa B signaling pathway.⁶⁰ Recently, NRP-1 was identified in adipose-tissue M Φ protecting from metabolic syndrome by favoring fatty acid uptake and β -oxidation away from pro-inflammatory M1 polarization and glycolysis.⁶¹ In addition, in a model of a neurodevelopmental disorder, brown adipose-tissue M Φ control sympathetic tissue innervation critical for thermogenesis via the plexin-semaphorin pathway.³⁵

The microbial composition of feces from HSCR patients with enterocolitis is shifted toward opportunistic pathogens such as *Candida albicans* and *Clostridium difficile*.^{1,62} In our study, none of the patients were diagnosed with enterocolitis at the time of the pull-through surgery. However, higher baseline frequencies of Th17 cells and IL23 might promote *C difficile* infection, as was recently postulated.⁶³ Compared with high-fiber colonic tissue, low-fiber tissue was associated with higher levels of *S aureus* previously reported to be associated with an increased Th17 response.⁶⁴ In contrast, Clostridiales Family_XI was up-regulated more than 2 log2 fold in high-fiber tissue compared with low-fiber tissue, which was reported to be associated with a decreased risk of *C difficile* infection and necrotizing enterocolitis in pre-term children.⁶⁵ In our study, differential bacterial analysis was limited because of the small sample size and high variability within the groups. The fact that we analyzed bacterial communities in colonic tissue rather than feces further limited the data analysis.

Overall, 9 of 42 patients developed HSCR-associated enterocolitis in the year after surgery. Interestingly, development of enterocolitis was significantly associated with cesarean delivery at birth of the infant in the prospective HSCR patient cohort. Microbial composition in children delivered by cesarean section is known to be associated with skin commensals such as *Staphylococcus*, whereas the microbiome in children delivered by vaginal birth mode is characterized by vaginal bacteria, eg, *Bifidobacteria* and *Lactobacillus*.⁶⁶ However, because cesarean section was not a significant risk factor in the retrospective patient cohort, its role in enterocolitis development needs to be further examined. Analyzing the correlation of fiber phenotype with enterocolitis development in the year after surgery showed a higher incidence for low-fiber phenotype (78%) than high-fiber phenotype (22%) in patients developing enterocolitis. The result was validated in a retrospectively analyzed HSCR patient cohort and showed a significant incidence of 86% (low-fiber phenotype) versus 14% (high-fiber phenotype) developing enterocolitis. In the prospective cohort, the low-fiber phenotype was not significantly associated with the outcome enterocolitis, most likely because of the small number of patients who experience this outcome as well as an unequal distribution of the low-fiber/high-fiber phenotype. When pooling the prospective and the retrospective dataset together, n = 23 had enterocolitis, and n = 48 did not have this outcome. Patients with the low-fiber phenotype experienced significantly more enterocolitis than those

with the high-fiber phenotype ($n = 19$ versus $n = 4$, $P = .020$). This finding indicates an association between a low-fiber phenotype and the development of enterocolitis in patients with Hirschsprung disease. Interestingly, in HSCR mouse models using *EndrB*-deficient mice, no mucosal nerve fibers were detected, and the mice exhibited microbial dysbiosis leading to enterocolitis.⁶⁷

The absence of mucosal AChE⁺ fibers could therefore serve as a predictive marker for enterocolitis and improve personalized patient management. With the current postoperative therapeutic management, clinicians react to inflammatory bowel situations only at the time point of enterocolitis onset. Using the fiber phenotype as a prognostic marker for the risk of enterocolitis, clinicians could directly react after pull-through surgery to prevent postoperative enterocolitis. Possible therapies include high-volume enemas, antibiotic interval treatment, prebiotic and probiotic therapy, as well as dietary adaptations. In addition, interventional surgical corrections may be considered. For instance, it is still unclear how the neuronal phenotype of a resected colon segment might predispose for enterocolitis development. It has been reported that colonic inflammatory Th17 cells migrate to neighboring mesenteric lymph nodes, triggering enterocolitis development. Because the mesentery is generally not removed during surgery, this could explain why patients may develop enterocolitis after removal of affected aganglionic colon segments. Using the fiber phenotype as a prognostic enterocolitis marker would enable possible resection of the neighboring mesentery lymph nodes/tissue as a strategy to prevent enterocolitis. Furthermore, immunotherapies targeting IL17 or IL23 rather than TNF- α could open new therapeutic treatment options.

The study is limited by its correlative nature requiring further investigations and validations. The fiber phenotype we investigated reflects the situation at the time point of pull-through surgery. It is unclear which factors drive the different innervation pattern between low-fiber and high-fiber tissue. There could be certain dietary or microbial triggers inducing mucosal fiber sprouting into the LP close to epithelial crypts in high-fiber tissue. A recent publication suggested a direct effect of the microbiome on gut extrinsic sympathetic neurons mediated by distal intestine-projecting afferent vagal neurons.⁶⁸ However, when analyzing data from the parent questionnaire, no significant difference in diet or domestic environment known to influence the microbial composition (eg, living area, siblings, pets) could be determined. On the other hand, one could assume that the low-fiber phenotype is a result of fiber loss due to epithelial barrier disruption resulting in tissue and neuroinflammation. However, we did not detect lower expression of epithelial tight junction proteins in low-fiber tissue, and we did not observe a higher bacterial translocation into low-fiber compared with high-fiber tissue. Although the origin of the fiber phenotype stays elusive, we suggest that the presence of neuronal cholinergic innervation in the colon might help to maintain a tolerogenic anti-inflammatory immune cell status to prevent excessive immune responses and tissue pathology. The involved cell types and

mechanisms as well as microbial contributions remain to be further investigated.

Using an HSCR patient cohort lacking the ENS, we showed that mucosal AChE⁺ nerve fibers associate with M Φ and correlate with reduced type-17 immune response, possibly mediated by reduced M Φ -dependent IL23 expression. HSCR patients lacking mucosal nerve fibers in the distal colon had a higher risk of developing postoperative enterocolitis. The mucosal fiber phenotype could serve as a new prognostic marker for HSCR-associated enterocolitis risk, offering personalized patient care and future therapeutic options.

Materials and Methods

Patients and Human Specimens

A total of 44 children (median age, 5 months) with HSCR as well as miscellaneous intestinal diseases (non-HSCR, control group) were enrolled in a prospective multicenter study conducted in Switzerland and Germany. The study was approved by the Ethics Committees of Northwest/Central Switzerland (EKNZ 2015-049) and the Medical Faculty Heidelberg (S-388/2015). The study was registered at www.clinicaltrials.gov (accessing number NCT03617640) and was performed according to the Declaration of Helsinki. After obtaining consent, fresh unfixed colonic tissue was collected in the operating room. For histologic analysis, a longitudinal strip of resected colonic tissue was immediately snap-frozen. Tissue for RNA analysis was stored in RNAlater (Qiagen, Hilden, Germany) or immediately frozen on dry ice. Tissue for FACS analysis was kept on ice in Hanks' balanced salt solution supplemented with 100 U penicillin, 0.1 mg/mL streptomycin, 0.25 μ g/mL amphotericin B, and 40 μ g/mL gentamycin and was processed in less than 24 hours. The HSCR group included patients with short-segment ($n = 31$), long-segment ($n = 6$), and total ($n = 7$) colonic aganglionosis. Surgery was performed according to the Swenson or Soave procedures (Table 1). The length of aganglionosis was determined intraoperatively by mapping biopsies and postoperatively in the resected tissue via enzyme-histochemical staining. Tissue staining and assessment were performed by the pathology units of the respective clinics (Table 7). Ganglionic tissue was characterized by the presence of intrinsic nerve cell bodies. The presence of intrinsic nerve cell bodies (ganglia) was detected by several enzyme histochemical stainings: lactic dehydrogenase, succinic dehydrogenase, NOS, nicotinamide adenine dinucleotide phosphate, and immunohistochemical calretinin staining. Aganglionic tissue was characterized by the lack of intrinsic cell bodies and presence of extrinsic nerve fibers in the distal colon.

Extrinsic nerve fibers were detected by enzyme histochemical AChE staining. Study group characteristics (clinical and nonclinical variables) were evaluated via a parent questionnaire. Postoperative symptoms (constipation, incontinence, enterocolitis, and pain) as well as postoperative treatments (laxative, enema, Botox, antibiotics, colonic irrigation, and prebiotics/probiotics) were evaluated from medical records 1 year after surgery.

Table 7. Enzyme Histochemistry Performed at the Different Pathology Units of Recruiting Clinics Used for HSCR Diagnosis

Pathology unit	Detection of ganglia	Detection of extrinsic nerve fibers
Basel, Freiburg, Karlsruhe	LDH, NOS, SDH	AChE
Zürich	LDH	AChE
Bern	LDH, NOS	AChE
St Gallen	SDH	AChE
Lausanne	LDH	AChE
Heidelberg	Calretinin	AChE
Düsseldorf	NADPH, LDH	AChE

LDH, lactic dehydrogenase; NADPH, nicotinamide adenine dinucleotide; SDH, succinic dehydrogenase.

Enterocolitis was defined on the basis of at least 3 of the following criteria: diarrhea (>3×/day), vomiting, temperature >38.5°C, antibiotics, hospitalization, abdominal distention, and high inflammatory blood parameters (ie, leukocytes, C-reactive protein). For the retrospective cohort analysis, we included HSCR patients diagnosed and treated at the University Children's Hospital Basel between 2003 and 2018. Patients were identified using International Classification of Diseases, 10th version diagnosis Q43.1. Swiss roll cryosections (5 μm) from resected distal aganglionic colon were provided by the Department of Pathology, University Hospital Basel, Basel, Switzerland. Fiber scoring was performed using beta III tubulin immunohistochemistry and evaluated in a double-blind fashion by 3 individuals. Demographic and clinical data were extracted from medical records. Enterocolitis was defined on the basis of the same criteria as in the prospective cohort study. The study was approved by the Ethics Committee of North-West Switzerland (EKNZ 2019-01406).

Immunohistochemistry and Nerve Fiber Scoring

Longitudinal colonic strips were washed in ice-cold phosphate buffered saline (PBS) and embedded as a Swiss roll in Tissue-Tek O.C.T. Compound (Sakura, Osaka, Japan). Cholinergic nerve fibers were visualized in 5-μm cryosections using mouse immunoglobulin (Ig)G2b anti-human AChE (Abcam, Cambridge, UK) or mouse IgG2a anti-human beta III tubulin antibody together with an anti-mouse HRP-AEC staining kit (R&D Systems, Minneapolis, MN) according to instruction manuals. Slides were automatically scanned using an Olympus (Tokyo, Japan) BX63 motorized brightfield microscope using a 10× objective. Presence of extrinsic nerve fibers in mucosal regions of the distal aganglionic colon was evaluated semiquantitatively in a double-blind investigation by 4 individuals. Mucosal regions were classified into 4 different fiber innervation grades according to absent, low, intermediate, and high innervation density (Figure 8A).²⁵ Innervation grades 1 and 2 were grouped into low-fiber and 3 and 4 were grouped into high-fiber HSCR

patients. For the quantitative measure of the AChE⁺ nerve fibers in the mucosal regions, images were analyzed using brightfield microscope and CellSens Dimension 2.2 Software (Olympus). On average, 6 cropped regions of interest containing 10 epithelial crypts from distal colon, resulting in 60 crypts per patients, were analyzed. In total, 12 patients (3 patients per innervation grade) were chosen according to the visual scoring. A defined manual threshold was applied on each cropped image, and object counts were obtained by the Olympus CellSens dimension software (Figure 2).

Isolation of Mononuclear Cells From Colonic Tissue

Colonic specimens were separated into rectum, sigmoid colon, descending colon, transverse colon, and ascending colon (distal to proximal) according to the length of the resected colon.⁶⁹ Excess fat was removed, and muscle layers were stripped from the mucosa. Mucosa and muscle tissue were minced and digested separately with collagenase D (1 mg/mL) and DNase I (4 μg/mL; both Roche Diagnostics, Basel, Switzerland) in complete medium (RPMI-1640 supplemented with 10% fetal calf serum, 200 U penicillin, 0.2 mg/mL streptomycin, 0.5 μg/mL amphotericin B, 80 μg/mL gentamycin, and 10 mmol/L HEPES) at 37°C for 1 hour under vigorous shaking. Digestion suspension was filtered through a 100-μm cell strainer, and cells were washed in complete medium. Suspension cells were resuspended in 20% Percoll (Pharmacia, Piscataway, NJ) (3 mL) and underlaid with 40% Percoll and 70% Percoll (3 mL of each). Mononuclear cells and epithelial cells were purified from the 40%/70% and the 20%/40% Percoll interface, respectively. Mononuclear cells were used freshly or were cryopreserved for further analysis. Isolated epithelial cells were immediately resuspended in RLT Lysis buffer and cryo stored until further analysis.

Flow Cytometry and FACS

For intracellular cytokine detection, cells were restimulated in complete medium with phorbol 12-myristate 13-acetate (150 ng/mL; Sigma-Aldrich, St Louis, MO) and ionomycin (750 ng/mL; Sigma-Aldrich) in the presence of GolgiStop and Brefeldin A (BD Biosciences, Franklin Lakes, NJ) for 4 hours at 37°C in a humidifying atmosphere (Table 5). Viability was determined by using LIVE/DEAD Fixable Near-IR dead cell stain (Thermo Fisher, Waltham, MA). Cell surface markers were stained extracellularly (15 min, 4°C) in FACS buffer (PBS supplemented with 2% fetal calf serum), whereas cytokines and transcription factors were detected intracellularly using Cytofix/Cytoperm (BD Biosciences) or Foxp3/transcription factor staining buffer set (eBioscience, San Diego, CA), respectively. Unspecific Fcγ receptor binding was blocked by human Fc block (CD16/CD32). Lineage cocktail for ILCs contained markers for T cells (CD3, TCRα/β; TCRγ/δ), NK T cells (CD56), B cells (CD19), dendritic cells, monocytes, MΦ (CD11c, CD14, CD16), and mast cells (FcγRI). Cells were analyzed using FACS Canto II (BD Biosciences) and FlowJo software (TreeStar Inc, Ashland, OR). MΦ were sorted as viable

CD45+ HLA+ CD64+ using FACS Aria cell sorter flow cytometry (BD Biosciences). Gating strategy is depicted in Figure 15. Table 8 details the human specific antibodies.

RNA Isolation and qRT-PCR

Colonic tissue samples (maximum 30 mg) were homogenized in RLT lysis buffer containing 1% 2-mercaptoethanol (Sigma-Aldrich) using a tissue disruptor (IKA). Total RNA from tissue or cells was isolated using the RNeasy Plus mini kit (Qiagen) and was reverse-transcribed using GoScript Reverse Transcription System (Promega, Madison, WI). Subsequently, qRT-PCR was done using the ViiA7 RT-PCR system (Thermo Fisher Scientific) and FastStart Universal SYBR Green Master (Roche Diagnostics) according to the manufacturers' instructions. Relative gene expression was calculated using the $2^{-\Delta\Delta CT}$ method, with β 2-microglobulin as housekeeping gene, and results were multiplied by a factor of 1000. Primer pairs were designed according to exon junction span using the clone manager software (Sci-Ed Software, Westminster, CO). Table 9 details the human-specific primer pairs.

Generation of Blood-Derived M1 and M2 M Φ

Peripheral blood mononuclear cells (PBMCs) from healthy adult volunteers were isolated using the SepMate/Lymphoprep system (Stemcell, Vancouver, Canada) according to the user manual. For monocyte attachment, PBMCs were resuspended in RPMI (supplemented with 10% fetal calf serum, 200 U penicillin, and 0.2 mg/mL streptomycin) and seeded into T-75 flasks for 2 hours at 37°C in a humidifying atmosphere. The attached monocytes were washed twice with PBS and then cultured for 10 days in M1 or M2 Macrophage Generation Medium DXF (PromoCell, Heidelberg, Germany) according to the manufacturer's instructions. On day 10, cells were detached by adding Accutase cell detachment solution (Sigma-Aldrich), washed twice with RPMI, and used for further applications.

T-Cell Conversion Assay

Autologous naive CD4 T cells were isolated from PBMCs using EasyStep Human naive CD4+ T cell Isolation Kit (Stemcell) according to instruction manuals. M1 or M2 M Φ (10^4 /well/200 μ L) were co-cultured with autologous naive CD4+ T cells (10^5 /well/200 μ L) in the presence of 5 μ g/mL anti-human CD3 for 6 days at 37°C in a humidifying atmosphere. Alternatively, CD4+ T cells were activated using anti-human CD3/CD28 activation Dynabeads (Life Technologies, Carlsbad, CA) in a 1:1 ratio. For T-helper cell differentiation, we added the following cytokines: IL2 (5 ng/mL) and TGF- β 1 (2 ng/mL) for Treg conversion and TGF- β 1 (2 ng/mL) and IL6 (10 ng/mL) for Th17 differentiation. All recombinant human cytokines were purchased from Peprotech (Rocky Hill, NJ). On day 6, T cells were separated from M Φ or Dynabeads into a new well and restimulated with phorbol 12-myristate 13-acetate (150 ng/mL) and ionomycin (750 ng/mL) in the presence of GolgiStop and Brefeldin A for 4 hours at 37°C in a humidifying atmosphere. T-cell subsets were subsequently analyzed by flow

cytometry using fluorescent antibodies against human TCR α/β , CD4, and IL17/Ror γ t or CD25/Foxp3 for Th17 and Treg cell identification. Cytokines and transcription factors were detected intracellularly using transcription factor buffer set (BD Biosciences) according to the manufacturer's instructions. Frequencies of single subsets were determined as percentages of viable CD4/TCR α/β positive T cells. Ratios of Th17/Treg frequencies were calculated.

Immunofluorescence and Co-localization Studies

For fluorescence staining of immune cells and cholinergic fibers, we established a modified protocol of the anti-mouse HRP-AEC staining kit (R&D). All steps were performed at room temperature. Between all steps, the tissues were washed 3 times for 10 minutes in PBS, and antibodies/streptavidin/4',6-diamidino-2'-phenylindole dihydrochloride (DAPI) were diluted in antibody diluent. Briefly, cryosections (5 μ m) were fixed with 4% paraformaldehyde for 5 minutes, followed by a blocking step with serum blocking reagent (15 minutes). Subsequently, avidin and biotin were blocked using Avidin Blocking Reagent (15 minutes), followed by Biotin Blocking Reagent (15 minutes). Primary antibodies were incubated for 1 hour and secondary antibodies for 45 minutes at room temperature. CD64, AChE, beta3tubulin, TH, nNOS, S100b, and VACHT were detected by secondary antibodies goat anti-mouse IgG1, IgG2a, or IgG2b labeled with A488, A555, A647, or biotin, as indicated. VIP was detected by anti-guinea pig A555. IL23p19 was directly phycoerythrin-labeled, and CD3 was directly A488-labeled. Biotin was visualized by streptavidin-Cy3 incubation for 30 minutes. Finally, nuclei were visualized by DAPI staining (3 minutes; 0.5 μ g/mL), and slides were mounted using Prolong Diamond Antifade Mountant (Life Technologies). Secondary antibody controls were included as negative controls. Images were taken by a fluorescence microscope (BX43 Olympus) and analyzed using CellSense (Olympus) and Fiji. Table 8 details the antibodies used for histology. Fast-scanning confocal microscopy was performed with a Zeiss (Oberkochen, Germany) LSM880 Airyscan inverted system. Images were acquired and processed using Zen Black with a 63 \times plan apochromatic oil immersion objective DIC M27(NA1.4) using the 3 respective Ar-lasers 561 nm, 488 nm, and 405 nm in 4 frames average fast mode. The acquisition parameters and settings of the images were verified for the absence of crosstalk between Green and Red excitation, and gain of the different lasers was always set at the same values for all acquisitions. Negative staining controls (secondary antibodies only) were used to determine pixel intensity background for the quantification. Images of high-fiber and low-fiber tissues were used for acquisition. Using a Fiji software macro, we quantified the co-localization pixel intensity between M Φ (or T cells) and AChE fibers. Briefly, images were created by multiplying and subsequent automated thresholding of the respective channels. Regions of interest containing M Φ (or T cells) were manually annotated in the raw data. The sums of co-localized pixel values contained within

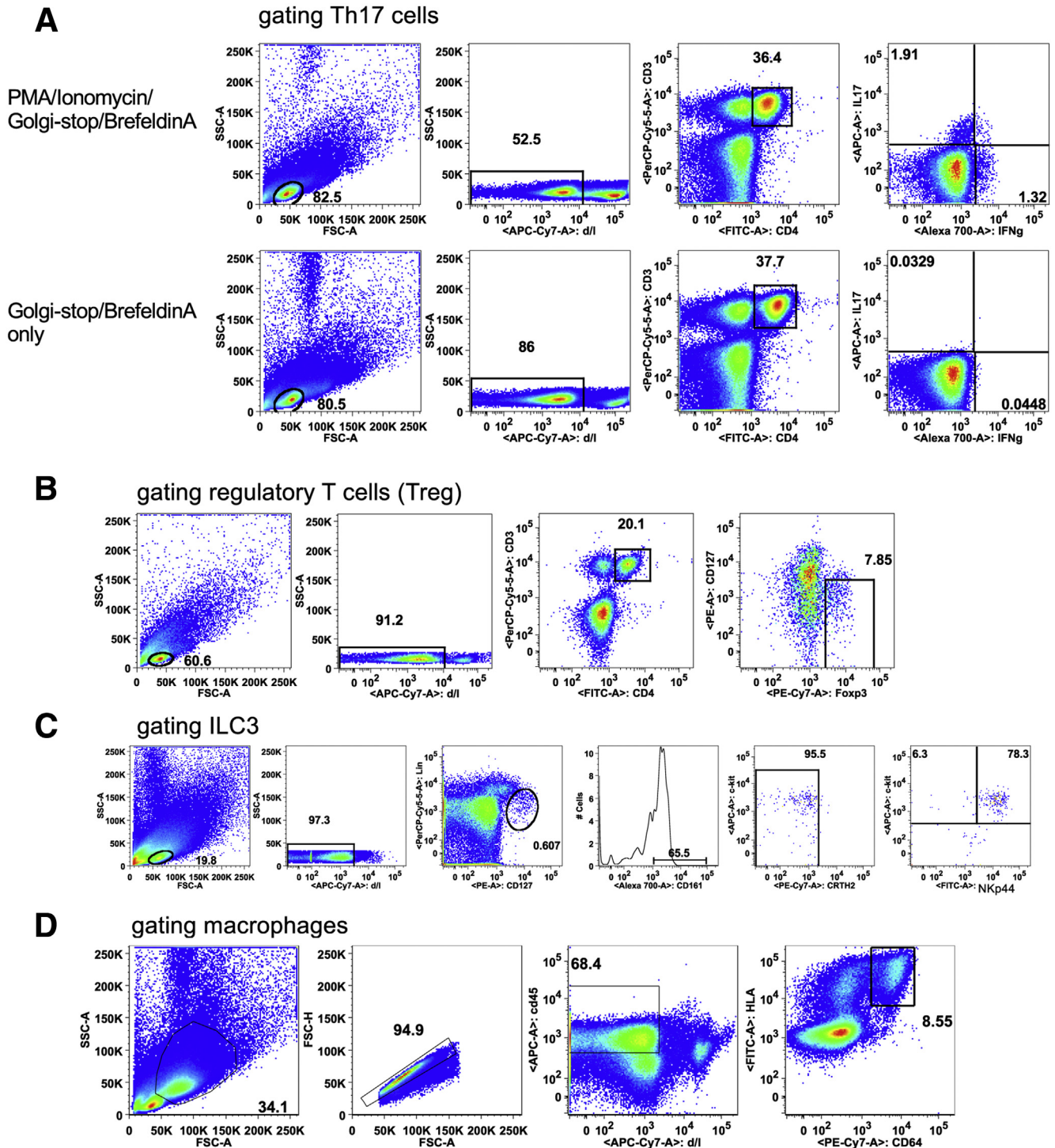


Figure 15. Gating strategy for flow cytometric analysis and cell sorting. (A–D) Representative gating strategies for FACS analysis of LP mononuclear cells from HSCR and control patients. (A) Th17 cells were evaluated in viable $CD3^+ CD4^+$ lymphocytes restimulated with phorbol 12-myristate 13-acetate (PMA)/ionomycin in the presence of GolgiStop and Brefeldin A. Unstimulated lymphocytes (Golgi-stop/Brefeldin A only) served as negative control. (B) $CD127^+ Foxp3^+$ Tregs were gated in viable $CD3^+ CD4^+$ lymphocytes. (C) Subsets of ILC3 were detected in viable $lin^- CD127^+ CD161^+ CRTH2^-$ lymphocytes. ILC3 NCR^+ were defined as $c-kit^+ NKp46^+$ and ILC3 NCR^- as $c-kit^+ NKp46^-$. (D) Macrophage gating strategy for FACS analysis as well as for cell sorting. $HLA^+ CD64^+$ macrophages were detected in viable $CD45^+$ leukocytes.

100–200 annotated M Φ (or T cells) per patient tissue were measured on a sum projection image. Data are shown as raw integrated density.

For the quantification of IL23, images recorded under a $20\times$ objective were analyzed using CellSense Software (Olympus) and Cellprofiler-3.1.9. To quantify IL23+ M Φ in

Table 8.Antibodies for FACS and Histology

Name	Clone	Fluorochrome	Supplier	Catalog no.	RRID	
Antibodies for flow cytometry						
CD3	SK7	PerCP	BioLegend	344814	AB_10639948	
HLA-DR	L243	FITC	eBioscience	11-9952-42	AB_2572542	
CD45	HI30	APC	BD Biosciences	555485	AB_398600	
CD14	HCD14	PerCP	BioLegend	325632	AB_2563328	
CD64	10.1	PE-Cy7	BioLegend	305022	AB_2561584	
CD11c	3.9	Alexa700	eBioscience	56-0116-42	AB_10547281	
CD4	RPA-T4	FITC	BD Biosciences	555346	AB_395751	
CD127	A019D5	PE	BioLegend	351304	AB_10720185	
CD25	BC96	Alexa 647	BioLegend	302618	AB_493045	
NKp44	p44-8	BB515	BD Biosciences	565099	AB_2739067	
CD11c	3.9	PerCP/Cy5.5	BioLegend	301624	AB_10640733	
CD19	HIB19	PerCP	BioLegend	302228	AB_893272	
CD56	HCD56	PerCP	BioLegend	318342	AB_2561865	
FcεRI	AER-37	PerCP	Novus Biologicals	NBP1-43278PCP	AB_10006605	
TCR α/β	IP26	PerCP/Cy5.5	BioLegend	306724	AB_2563002	
TCR γ/δ	B1	PerCP/Cy5.5	BioLegend	331224	AB_2563013	
CD117 (c-kit)	104D2	APC	BioLegend	313206	AB_314985	
CD294 (CRTH2)	BM16	PE-Cy7	BioLegend	350118	AB_2562470	
CD161	HP-3G10	Alexa 700	BioLegend	339942	AB_2565870	
IL17A	eBio64DEC17	APC	eBioscience	17-7179-42	AB_1582221	
IFN-γ	B27	Alexa 700	BioLegend	506516	AB_961351	
Roryt	Q21-559	Alexa 488	BD Biosciences	563621	AB_2738325	
Foxp3	PCH101	PE-Cy7	eBioscience	25-4776-42	AB_10804638	
CD16/CD32 (Fc block)		purified	BD Biosciences	564219	AB_2728082	
Name	Clone	Fluorochrome	Host-subtype	Supplier	Catalog no.	RRID
Primary antibodies for histology						
CD64	10.1	purified	mouse IgG1	BioLegend	305002	AB_314486
CD3	UCHT1	Alexa 488	mouse IgG1	BioLegend	300454	AB_2564149
AChE	HR2	purified	mouse IgG2b	Abcam	ab2803	AB_303316
Beta III tubulin	2G10	purified	mouse IgG2a	Abcam	ab78078	AB_2256751
Beta III tubulin	GT11710	purified	mouse IgG2b	Genetex	GTX631836	AB_2814952
TH	1A5	purified	mouse IgG2a	Invitrogen	MA1-24654	AB_795666
nNOS	16/nNOS/NOS type I	purified	mouse IgG2a	BD Bioscience	610308	AB_397700
S100b	11C12E12	purified	mouse IgG1	BioLegend	676603	AB_2734531
VIP	polyclonal	purified	guinea pig	Peninsula Laboratories	sc-25347	AB_628439
VACHT	S6-38	purified	mouse IgG1	Thermo Fisher Scientific	MA5-27662	AB_2735407
IL23p19	23dcdp	PE	mouse IgG2b	eBioscience	12-7823-41	AB_10669562

tissues of different patient groups (4 low-fiber, 4 high-fiber), 4–8 regions per patient from rectum and sigmoid colon were used. Primary objects were defined by nuclear DAPI staining. Secondary object was defined by extracellular CD64 expression using the watershed module after applying a global

threshold for improved cell identification. IL23⁺ cells were identified as a second primary object (IL23⁺), using Three classes Otsu thresholding method and subsequently related to CD64 MΦ. Frequencies of IL23⁺ MΦ (IL23⁺ CD64⁺) were shown as the percentage of total MΦ.

Table 9.List of Primers

Gene	Forward sequence 5'-3'	Reverse sequence 5'-3'
AChE	CAT CTT TGG GAT CCC CCT GG	TCA TTG GGA TCC CCT GTG C
CX3CR1	CAT CGT GGT CTT TGG GAC TG	TTG GTG AGG GCA AAC ACT AC
CCR2	ATA CCA GGA CTG CCT GAG AC	CGC TCT CGT TGG TAT TTC TG
Occludin	ATG GAC TGC GTC ACG CAG AG	CCA CAA ACA TGG CCA GGA AG
ZO-1	AGC ACA GCA ATG GAG GAA AC	GGT CCT CCT TTC AGC ACA TC
β2M	CAG CGT ACT CCA AAG ATT CA	GAA TGC TCC ACT TTT TCA AT

Table 10. Statistical Analysis of Protein Expression

FACS analysis	Th17	Treg	Th17/Treg ratio	ILC3 NCR-	ILC3 NCR+	CD14+	CD11c+	Th17 % total	Treg % total	Th17/Treg ratio % total	CD14 % total
Fiber-low vs fiber-high	0.0203 ^a	0.0874	0.0699	0.2455	0.5744	0.0173 ^a	0.3571	0.0085 ^a	0.091	0.4842	0.4998
Fiber-low vs DC AG	0.0051 ^a	0.0846	0.1079	0.5821	0.4535	0.5086	0.6999	0.0767	0.6356	0.0934	0.5709
Fiber-low vs DC G	0.015 ^a	0.1208	0.1874	0.0809	0.8556	0.5149	0.0905	0.0686	0.0498 ^a	0.7638	0.8804
Fiber-low vs DC control	0.0875	0.2958	0.244	0.8351	0.9763	0.1437	0.7554	0.0984	0.3886	0.7609	0.7651
Fiber-high vs DC AG	0.5211	0.0046 ^a	0.9658	0.6409	0.8335	0.0128 ^a	0.2791	0.5518	0.072	0.045 ^a	0.9649
Fiber-high vs DC G	0.773	0.008 ^a	0.762	0.5306	0.7657	0.1685	0.4438	0.5831	0.7046	0.4274	0.68
Fiber-high vs DC control	0.9386	0.0432 ^a	0.9276	0.5975	0.7073	0.8401	0.7589	0.8482	0.776	0.8665	0.8737
DC AG vs DC G	0.7391	0.9554	0.8068	0.3049	0.6322	0.2763	0.0845	0.9652	0.0411 ^a	0.2494	0.7288
DC AG vs DC control	0.6751	0.8678	0.9567	0.8651	0.606	0.0812	0.5897	0.7844	0.2784	0.1417	0.9053
DC G vs DC control	0.8828	0.906	0.8844	0.3349	0.8844	0.3851	0.3779	0.8119	0.5727	0.6371	0.8696
Fiber-low vs muscle						0.0031 ^a	0.1598				0.0052 ^a
Fiber-high vs muscle						0.4106	0.6127				0.0448 ^a
DC AG vs muscle						0.0026 ^a	0.1371				0.053
DC G vs muscle						0.0437 ^a	0.8063				0.024 ^a
DC control vs muscle						0.4067	0.4946				0.0864
Luminex analysis	IL17	IL22	IL6	IL1b	IL23	TNF- α	IFN- γ				
Fiber-low vs fiber-high	0.1902	0.6819	0.1494	0.3519	0.2586	0.4577	0.7052				
Fiber-low vs DC AG	0.2889	0.9629	0.5148	0.1978	0.4495	0.3657	0.664				
Fiber-low vs DC G	0.5562	0.2818	0.1644	0.4058	0.7027	0.1131	0.4937				
Fiber-low vs DC control	0.8747	0.4205	0.7879	0.872	0.6957	0.5716	0.9371				
Fiber-high vs DC AG	0.0485 ^a	0.7042	0.0815	0.0634	0.1215	0.1671	0.4962				
Fiber-high vs DC G	0.5552	0.5609	0.9919	0.9494	0.2245	0.4559	0.7873				
Fiber-high vs DC control	0.4928	0.3191	0.2469	0.6592	0.8588	0.9599	0.7455				
DC AG vs DC G	0.1694	0.3471	0.0893	0.0783	0.7738	0.039 ^a	0.3523				
DC AG vs DC control	0.4097	0.4829	0.8616	0.3299	0.4575	0.2751	0.8219				
DC G vs DC control	0.8142	0.1568	0.2554	0.6977	0.576	0.6088	0.5919				

^aStatistically significant value.

Luminex Analysis and Enzyme-Linked Immunosorbent Assays

Colonic tissues samples were homogenized in Tissue Extraction Reagent I (100 μ L/10 mg; ThermoFisher) containing protease inhibitor cocktail (Sigma-Aldrich) using a tissue disruptor (IKA). Concentrations (pg/mL) of IL6, IL22, IL1 β , TNF- α , and IL17 were determined using MILLI-PLEX_{MAP} Human Cytokine/Chemokine/Growth Factor Panel A Assay (Millipore Sigma, St Louis, MO) and Luminex xMAP technology (MAGPIX) according to the manufacturers'

instructions. Samples were measured using xPONENT for MAGPIX software. IL23 was determined in tissue lysates using Human IL-23 ELISA Ready-Set-Go according to the manufacturer's instructions. IL-23 ELISA was measured using a Synergy H4 Hybrid Reader and GEN5 2.00 software (BioTek, Winooski, VT).

16S rRNA FISH

The FISH procedure was performed in 5- μ m rectum/sigmoid colon Swiss roll cryosections. We used Cy3-labeled

EUB338 probe (GCT GCC TCC CGT AGG AGT) complementary to bacteria-specific 16S rRNA region as well as NON338 probe (ACT CCT ACG GGA GGC AGC), an oligonucleotide complementary to the probe EUB338, to control for nonspecific binding. Colonic tissue sections were fixed with 4% paraformaldehyde for 20 minutes on ice, followed by a wash step in PBS. Slides were dipped into ice-cold methanol before hybridization in hybridization buffer (20 mmol/L Tris-HCl, 0.9% NaCl, 0.1% sodium dodecyl sulfate) at 48°C for 16 hours. Slides were washed twice in hybridization wash buffer (20 mmol/L Tris-HCl, 0.9% NaCl, pH 7.2) for 30 minutes at 48°C and subsequently mounted with ProLong Gold Antifade Mountant with DAPI (Life Technologies) and evaluated with a fluorescence microscope (BX43 Olympus). Images were analyzed using CellSense Software (Olympus) and Fiji software. To quantify the bacterial translocation in the different patient groups, 4–6 regions per picture from rectum and sigmoid colon were used, and corresponding sites were used for anti-sense probe. On average, 2000 DAPI+ cells/region were then processed using Cellprofiler software. In brief, primary objects were defined by nuclear DAPI staining. After masking the nuclei, a second primary object (Eub338_bacteria) based on nuclear Eub338 expression was defined and related to DAPI+ cells. Global Otsu two classes thresholding method was applied for DAPI nuclei staining, and manual thresholding for Eub338 was used before masking the nuclei to subtract the background. The anti-sense probe was running in parallel under the same pipeline, and results were subtracted from the sense probe. Frequencies of translocated bacteria (16S rRNA⁺/DAPI⁺) were expressed as the percentage of total DAPI⁺ cells.

16S rDNA Gene Sequencing

For 16S rDNA microbial analysis, we used colonic cryosections (100 μm). Extraction, lysis, and DNA isolation were done using Fast DNA Stool Mini Kit (Qiagen) according to the manufacturer's instructions. Bead beating was run on a fastprep24 instrument (MP Biomedicals, Santa Ana, CA; 2 cycles of 45 seconds at speed 4, followed by 2 cycles of 45 seconds at speed 5) in 2 mL screwcap tubes containing 0.1 mm zirconia beads (0.3 g) and 2.3 mm zirconia beads (0.36 g). The whole raw extract was prepared for DNA isolation. Concentration of the isolated DNA was determined with PicoGreen measurement (Quant-iT PicoGreen dsDNA Assay Kit; Thermo Fisher), and integrity was checked by agarose gel electrophoresis.

The Illumina MiSeq (San Diego, CA) platform and a v2 500 cycles kit were used to sequence the PCR libraries. The produced paired-end reads that passed Illumina's chastity filter were subjected to de-multiplexing and trimming of Illumina adaptor residuals using Illumina's real-time analysis software included in the MiSeq reporter software v2.6 (no further refinement or selection). The quality of the reads was checked with the software FastQC version 0.11.7. The locus-specific V34 primers were trimmed from the sequencing reads with the software Cutadapt v1.14. Paired-end reads were discarded if the primer

could not be trimmed. Trimmed-forward and reverse reads of each paired-end read were merged to reform the sequenced molecule *in silico*, considering a minimum overlap of 15 bases using the software USEARCH version 10.0.240. Merged sequences were then quality-filtered, allowing a maximum of one expected error per merged read and also discarding those containing ambiguous bases. The remaining reads were denoised using the UNOISE algorithm implemented in USEARCH to form OTUs discarding singletons and chimeras in the process. OTUs were compared with the reference sequences of the SILVA 16S database, and taxonomies were predicted considering a minimum confidence threshold of 0.6 using the SINTAX algorithm implemented in USEARCH. Alpha diversity was estimated using the Richness (Observed), Shannon and Simpson indices. Beta diversity was calculated using the Unifrac distance method on the basis of normalized OTU abundance counts per sample. These sample distances were then used in a detrended correspondence analysis to reveal possible patterns of intersample relations. Alpha and beta diversity calculations and the rarefaction analysis were performed with the R software package phyloseq v1.22.3. To detect differentially abundant OTUs depending on collected sample metadata (eg, medication, environmental conditions), differential OTU analysis on normalized abundance counts was performed with the R software package DESeq2 v1.18.1. Libraries, sequencing, and data analysis described in this section were performed by Microsynth AG (Balgach, Switzerland).

RNA-seq Analysis

FACS sorted viable MΦ (300–3000 cells) as well as blood-derived M1 and M2 MΦ (100,000 cells) were used for RNA-seq analysis. RNA was isolated using RNeasy micro kit (Qiagen). RNA samples were quantified using Qubit 2.0 Fluorometer (Life Technologies), and RNA integrity was checked with Agilent TapeStation (Agilent Technologies, Palo Alto, CA). RNA library preparations, sequencing reactions, and initial bioinformatics analysis were conducted at GENEWIZ, LLC (South Plainfield, NJ). The SMART-Seq v4 Ultra Low input kit for sequencing was used for full-length cDNA synthesis and amplification (Clontech, Mountain View, CA) according to the manufacturer's protocol. Illumina Nextera XT library was used for library preparation. Briefly, cDNA was fragmented, and adaptors were added using transposase, followed by limited-cycle PCR to enrich and add index to the cDNA fragments. Final libraries were analyzed on the Agilent TapeStation for library sizing and quantified using the Qubit dsDNA HS assay kit and by qPCR using the KAPA library quantification kit. The sequencing libraries were multiplexed and clustered on 2 lanes of a flow cell. After clustering, the flow cell was loaded on the Illumina HiSeq instrument according to the manufacturer's instructions. The samples were sequenced using a 2×150 Paired End configuration. Image analysis and base calling were conducted by the HiSeq Control Software (HCS). Raw sequence data (.bcl files) generated from Illumina HiSeq were converted into fastq files and de-multiplexed using

Illumina's bcl2fastq 2.17 software. One mismatch was allowed for index sequence identification. After investigating the quality of the raw data, sequence reads were trimmed to remove possible adapter sequences and nucleotides with poor quality using Trimmomatic v.0.36. The trimmed reads were mapped to the human reference genome available on ENSEMBL using the STAR aligner v.2.5.2b. The STAR aligner uses a splice aligner that detects splice junctions and incorporates them to help align the entire read sequences. BAM files were generated as a result of this step. Unique gene hit counts were calculated by using featureCounts of the Subread package v.1.5.2. Only unique reads that fell within exon regions were counted. After extraction of gene hit counts, the gene hit counts table was used for downstream differential expression analysis. All statistical analyses were performed using R project software. Comparison of gene expression between the groups of samples was performed with the package DESeq2. The Wald test was used to generate *P* values and log₂ fold changes. Genes with adjusted *P* values <.05 and absolute log₂ fold changes >1 were regarded as differentially expressed genes for each comparison. The statistically significant set of genes was subjected to a gene ontology analysis by implementing the software GeneSCF. The mgi GO list was used to cluster the set of genes on the basis of their biological process and to determine their statistical significance. A PCA was performed using the plotPCA function of the DESeq2 R package. The plot shows the samples in a 2-dimensional plane spanned by their first 2 principal components. The top 500 genes, selected by highest row variance, were used to generate the plot.

Statistical Analysis

Data were analyzed using Prism GraphPad (San Diego, CA) 6.0 software and Stata (StataCorp 2015, Stata Statistical Software: Release 15; College Station, TX). Data are reported as the means ± standard error of the mean. Statistical significance was determined using one-way analysis of variance multiple comparison analysis, unpaired nonparametric two-tailed Mann-Whitney test, and unpaired *t* test (for M1/M2 MΦ). Differences were considered statistically significant with **P* ≤ .05, ***P* ≤ .01, ****P* ≤ .001, and *****P* ≤ .0001. Unless otherwise noted, figures show pooled patient data from several independent experiments or a representative of repeated experiments. The characteristics and risk factors of study participants were compared between low-fiber versus high-fiber HSCR patient groups and between subjects with enterocolitis versus no enterocolitis during follow-up by using two-sided Wilcoxon rank-sum test and χ^2 test, as appropriate.

Data Availability

The data sets generated and analyzed during the current study have been deposited in NCBI Sequence Read Archive under the accession code PRJNA552657 (RNA-seq datasets) and PRJNA550537 (16S rDNA datasets). All other study-related data are available from the corresponding author upon reasonable request.

All authors had access to the study data and reviewed and approved the final manuscript.

References

- Demehri FR, Halaweish IF, Coran AG, Teitelbaum DH. Hirschsprung-associated enterocolitis: pathogenesis, treatment and prevention. *Pediatr Surg Int* 2013; 29:873–881.
- Mattar AF, Coran AG, Teitelbaum DH. MUC-2 mucin production in Hirschsprung's disease: possible association with enterocolitis development. *J Pediatr Surg* 2003;38:417–421, discussion 421.
- Imamura A, Puri P, O'Briain DS, Reen DJ. Mucosal immune defence mechanisms in enterocolitis complicating Hirschsprung's disease. *Gut* 1992;33:801–806.
- Thomas DF, Fernie DS, Malone M, Bayston R, Spitz L. Association between *Clostridium difficile* and enterocolitis in Hirschsprung's disease. *Lancet* 1982;1:78–79.
- Bruder E, Terracciano LM, Passarge E, Meier-Ruge WA. [Enzyme histochemistry of classical and ultrashort Hirschsprung's disease]. *Pathologe* 2007;28:105–112.
- Wetherill C, Sutcliffe J. Hirschsprung disease and anorectal malformation. *Early Hum Dev* 2014;90:927–932.
- Kamijo K, Hiatt RB, Koelle GB. Congenital megacolon; a comparison of the spastic and hypertrophied segments with respect to cholinesterase activities and sensitivities to acetylcholine, DFP and the barium ion. *Gastroenterology* 1953;24:173–185.
- Meier-Ruge W, Lutterbeck PM, Herzog B, Morger R, Moser R, Scharli A. Acetylcholinesterase activity in suction biopsies of the rectum in the diagnosis of Hirschsprung's disease. *J Pediatr Surg* 1972;7:11–17.
- Meier-Ruge W, Hunziker O, Tobler HJ, Walliser C. The pathophysiology of aganglionosis of the entire colon (Zuelzer-Wilson syndrome): morphometric investigations of the extent of sacral parasympathetic innervation of the circular muscles of the aganglionic colon. *Beitr Pathol* 1972;147:228–236.
- Niemi M, Kouvalainen K, Hjelt L. Cholinesterases and monoamine oxidase in congenital megacolon. *J Pathol Bacteriol* 1961;82:363–366.
- Payette RF, Tennyson VM, Pham TD, Mawe GM, Pomeranz HD, Rothman TP, Gershon MD. Origin and morphology of nerve fibers in the aganglionic colon of the lethal spotted (ls/ls) mutant mouse. *J Comp Neurol* 1987;257:237–252.
- Devroede G, Lamarche J. Functional importance of extrinsic parasympathetic innervation to the distal colon and rectum in man. *Gastroenterology* 1974;66:273–280.
- Smith B. Myenteric plexus in Hirschsprung's disease. *P Roy Soc Med* 1967;60:803.
- Garrett JR, Howard ER, Nixon HH. Autonomic nerves in rectum and colon in Hirschsprung's disease: a cholinesterase and catecholamine histochemical study. *Arch Dis Child* 1969;44:406–417.
- Borovikova LV, Ivanova S, Zhang M, Yang H, Botchkina GI, Watkins LR, Wang H, Abumrad N, Eaton JW, Tracey KJ. Vagus nerve stimulation attenuates the systemic inflammatory response to endotoxin. *Nature* 2000;405:458–462.

16. Rosas-Ballina M, Olofsson PS, Ochani M, Valdes-Ferrer SI, Levine YA, Reardon C, Tusche MW, Pavlov VA, Andersson U, Chavan S, Mak TW, Tracey KJ. Acetylcholine-synthesizing T cells relay neural signals in a vagus nerve circuit. *Science* 2011;334:98–101.
17. Ghia JE, Blennerhassett P, Kumar-Ondiveeran H, Verdu EF, Collins SM. The vagus nerve: a tonic inhibitory influence associated with inflammatory bowel disease in a murine model. *Gastroenterology* 2006;131:1122–1130.
18. Di Giovangiulio M, Bosmans G, Meroni E, Stakenborg N, Florens M, Farro G, Gomez-Pinilla PJ, Matteoli G, Boeckxstaens GE. Vagotomy affects the development of oral tolerance and increases susceptibility to develop colitis independently of the alpha-7 nicotinic receptor. *Mol Med* 2016;22:464–476.
19. Matteoli G, Gomez-Pinilla PJ, Nemethova A, Di Giovangiulio M, Cailotto C, van Bree SH, Michel K, Tracey KJ, Schemann M, Boesmans W, Vanden Berghe P, Boeckxstaens GE. A distinct vagal anti-inflammatory pathway modulates intestinal muscularis resident macrophages independent of the spleen. *Gut* 2014;63:938–948.
20. Bastida G, Beltran B. Ulcerative colitis in smokers, non-smokers and ex-smokers. *World J Gastroenterol* 2011;17:2740–2747.
21. Bonaz B, Sinniger V, Hoffmann D, Clarencon D, Mathieu N, Dantzer C, Vercueil L, Picq C, Trocme C, Faure P, Cracowski JL, Pellissier S. Chronic vagus nerve stimulation in Crohn's disease: a 6-month follow-up pilot study. *Neurogastroenterol Motil* 2016;28:948–953.
22. Sinniger V, Pellissier S, Fauvelle F, Trocme C, Hoffmann D, Vercueil L, Cracowski JL, David O, Bonaz B. A 12-month pilot study outcomes of vagus nerve stimulation in Crohn's disease. *Neurogastroenterol Motil* 2020;32:e13911.
23. Payne SC, Furness JB, Burns O, Sedo A, Hyakumura T, Shepherd RK, Fallon JB. Anti-inflammatory effects of abdominal vagus nerve stimulation on experimental intestinal inflammation. *Front Neurosci* 2019;13:418.
24. Szyllberg L, Marszalek A. Diagnosis of Hirschsprung's disease with particular emphasis on histopathology: a systematic review of current literature. *Prz Gastroenterol* 2014;9:264–269.
25. Braczynski AK, Gfroerer S, Beschorner R, Harter PN, Baumgarten P, Rolle U, Mittelbronn M. Cholinergic innervation and ganglion cell distribution in Hirschsprung's disease. *BMC Pediatr* 2020;20:399.
26. Klapproth H, Reinheimer T, Metzén J, Munch M, Bittinger F, Kirkpatrick CJ, Hohle KD, Schemann M, Racke K, Wessler I. Non-neuronal acetylcholine, a signalling molecule synthesized by surface cells of rat and man. *Naunyn Schmiedeberg's Arch Pharmacol* 1997;355:515–523.
27. Pan J, Zhang L, Shao X, Huang J. Acetylcholine from tuft cells: the updated insights beyond its immune and chemosensory functions. *Front Cell Dev Biol* 2020;8:606.
28. Kuhl AA, Erben U, Kredel LI, Siegmund B. Diversity of intestinal macrophages in inflammatory bowel diseases. *Front Immunol* 2015;6:613.
29. Hadis U, Wahl B, Schulz O, Hardtke-Wolenski M, Schippers A, Wagner N, Muller W, Sparwasser T, Forster R, Pabst O. Intestinal tolerance requires gut homing and expansion of FoxP3+ regulatory T cells in the lamina propria. *Immunity* 2011;34:237–246.
30. Regoli M, Bertelli E, Gulisano M, Nicoletti C. The multifaceted personality of intestinal CX3CR1(+) macrophages. *Trends Immunol* 2017;38:879–887.
31. Dionne S, Duchatelier CF, Seidman EG. The influence of vitamin D on M1 and M2 macrophages in patients with Crohn's disease. *Innate Immun-London* 2017;23:557–565.
32. Muller PA, Koscsó B, Rajani GM, Stevanovic K, Berres ML, Hashimoto D, Mortha A, Leboeuf M, Li XM, Mucida D, Stanley ER, Dahan S, Margolis KG, Gershon MD, Merad M, Bogunovic M. Crosstalk between muscularis macrophages and enteric neurons regulates gastrointestinal motility. *Cell* 2014;158:1210.
33. Gabanyi I, Muller PA, Feighery L, Oliveira TY, Costa-Pinto FA, Mucida D. Neuro-immune interactions drive tissue programming in intestinal macrophages. *Cell* 2016;164:378–391.
34. De Schepper S, Stakenborg N, Matteoli G, Verheijden S, Boeckxstaens GE. Muscularis macrophages: key players in intestinal homeostasis and disease. *Cell Immunol* 2018;330:142–150.
35. Wolf Y, Boura-Halfon S, Cortese N, Haimon Z, Sar Shalom H, Kuperman Y, Kalchenko V, Brandis A, David E, Segal-Hayoun Y, Chappell-Maor L, Yaron A, Jung S. Brown-adipose-tissue macrophages control tissue innervation and homeostatic energy expenditure. *Nat Immunol* 2017;18:665–674.
36. Kolter J, Kierdorf K, Henneke P. Origin and differentiation of nerve-associated macrophages. *J Immunol* 2020;204:271–279.
37. Willemze RA, Welting O, van Hamersveld P, Verseijden C, Nijhuis LE, Hilbers FW, Meijer SL, Heesters BA, Folgering JHA, Darwinkel H, Blancou P, Vervoordeldonk MJ, Seppen J, Heinsbroek SEM, de Jonge WJ. Loss of intestinal sympathetic innervation elicits an innate immune driven colitis. *Mol Med* 2019;25:1.
38. Lim HY, Lim SY, Tan CK, Thiam CH, Goh CC, Carbajo D, Chew SHS, See P, Chakarov S, Wang XN, Lim LH, Johnson LA, Lum J, Fong CY, Bongso A, Biswas A, Goh C, Evrard M, Yeo KP, Basu R, Wang JK, Tan Y, Jain R, Tikoo S, Choong C, Weninger W, Poidinger M, Stanley ER, Collin M, Tan NS, Ng LG, Jackson DG, Ginhoux F, Angeli V. Hyaluronan receptor LYVE-1-expressing macrophages maintain arterial tone through hyaluronan-mediated regulation of smooth muscle cell collagen. *Immunity* 2018;49:1191.
39. Stakenborg N, Labeeuw E, Gomez-Pinilla PJ, De Schepper S, Aerts R, Goverse G, Farro G, Appeltans I, Meroni E, Stakenborg M, Viola MF, Gonzalez-Dominguez E, Bosmans G, Alpizar YA, Wolthuis A, D'Hoore A, Van Beek K, Verheijden S, Verhaegen M, Derua R, Waelkens E, Moretti M, Gotti C, Augustijns P, Talavera K, Vanden Berghe P, Matteoli G, Boeckxstaens GE. Preoperative administration of the 5-

- HT4 receptor agonist prucalopride reduces intestinal inflammation and shortens postoperative ileus via cholinergic enteric neurons. *Gut* 2018;68:1406–1416.
40. Cardoso V, Chesne J, Ribeiro H, Garcia-Cassani B, Carvalho T, Bouchery T, Shah K, Barbosa-Morais NL, Harris N, Veiga-Fernandes H. Neuronal regulation of type 2 innate lymphoid cells via neuromedin U. *Nature* 2017;549:277–281.
 41. Klose CSN, Mahlakoiv T, Moeller JB, Rankin LC, Flamar AL, Kabata H, Monticelli LA, Moriyama S, Putzel GG, Rakhilin N, Shen X, Kostenis E, Konig GM, Senda T, Carpenter D, Farber DL, Artis D. The neuropeptide neuromedin U stimulates innate lymphoid cells and type 2 inflammation. *Nature* 2017;549:282–286.
 42. Riol-Blanco L, Ordovas-Montanes J, Perro M, Naval E, Thiriot A, Alvarez D, Paust S, Wood JN, von Andrian UH. Nociceptive sensory neurons drive interleukin-23-mediated psoriasiform skin inflammation. *Nature* 2014;510:157–161.
 43. Kashem SW, Riedl MS, Yao C, Honda CN, Vulchanova L, Kaplan DH. Nociceptive sensory fibers drive interleukin-23 production from CD301b+ dermal dendritic cells and drive protective cutaneous immunity. *Immunity* 2015;43:515–526.
 44. Medina-Contreras O, Geem D, Laur O, Williams IR, Lira SA, Nusrat A, Parkos CA, Denning TL. CX3CR1 regulates intestinal macrophage homeostasis, bacterial translocation, and colitogenic Th17 responses in mice. *J Clin Invest* 2011;121:4787–4795.
 45. Agace WW, McCoy KD. Regionalized development and maintenance of the intestinal adaptive immune landscape. *Immunity* 2017;46:532–548.
 46. James KR, Gomes T, Elmentaite R, Kumar N, Gulliver EL, King HW, Stares MD, Bareham BR, Ferdinand JR, Petrova VN, Polanski K, Forster SC, Jarvis LB, Suchanek O, Howlett S, James LK, Jones JL, Meyer KB, Clatworthy MR, Saeb-Parsy K, Lawley TD, Teichmann SA. Distinct microbial and immune niches of the human colon. *Nat Immunol* 2020;21:343–353.
 47. Atarashi K, Nishimura J, Shima T, Umesaki Y, Yamamoto M, Onoue M, Yagita H, Ishii N, Evans R, Honda K, Takeda K. ATP drives lamina propria T(H)17 cell differentiation. *Nature* 2008;455:808–812.
 48. Thome JJ, Bickham KL, Ohmura Y, Kubota M, Matsuoka N, Gordon C, Granot T, Griesemer A, Lerner H, Kato T, Farber DL. Early-life compartmentalization of human T cell differentiation and regulatory function in mucosal and lymphoid tissues. *Nat Med* 2016;22:72–77.
 49. Teratani T, Mikami Y, Nakamoto N, Suzuki T, Harada Y, Okabayashi K, Hagihara Y, Taniki N, Kohno K, Shibata S, Miyamoto K, Ishigame H, Chu PS, Sujino T, Suda W, Hattori M, Matsui M, Okada T, Okano H, Inoue M, Yada T, Kitagawa Y, Yoshimura A, Tanida M, Tsuda M, Iwasaki Y, Kanai T. The liver-brain-gut neural arc maintains the Treg cell niche in the gut. *Nature* 2020;585:591–596.
 50. De Schepper S, Verheijden S, Aguilera-Lizarraga J, Viola MF, Boesmans W, Stakenborg N, Voytyuk I, Schmidt I, Boeckx B, Dierckx de Casterle I, Baekelandt V, Gonzalez Dominguez E, Mack M, Depoortere I, De Strooper B, Sprangers B, Himmelreich U, Soenen S, Guilliams M, Vanden Berghe P, Jones E, Lambrechts D, Boeckxstaens G. Self-maintaining gut macrophages are essential for intestinal homeostasis. *Cell* 2018;175:400–415 e13.
 51. Avetisyan M, Rood JE, Lopez SH, Sengupta R, Wright-Jin E, Dougherty JD, Behrens EM, Heuckeroth RO. Muscularis macrophage development in the absence of an enteric nervous system. *Proc Natl Acad Sci USA* 2018;115:4696–4701.
 52. Bosmans G, Appeltans I, Stakenborg N, Gomez-Pinilla PJ, Florens MV, Aguilera-Lizarraga J, Matteoli G, Boeckxstaens GE. Vagus nerve stimulation dampens intestinal inflammation in a murine model of experimental food allergy. *Allergy* 2019;74:1748–1759.
 53. van der Zanden EP, Snoek SA, Heinsbroek SE, Stanisor OI, Verseijden C, Boeckxstaens GE, Peppelenbosch MP, Greaves DR, Gordon S, De Jonge WJ. Vagus nerve activity augments intestinal macrophage phagocytosis via nicotinic acetylcholine receptor $\alpha 4\beta 2$. *Gastroenterology* 2009;137:1029–1039, 39 e1–e4.
 54. Klose CS, Artis D. Neuronal regulation of innate lymphoid cells. *Curr Opin Immunol* 2019;56:94–99.
 55. Keck S, Schmalzer M, Ganter S, Wyss L, Oberle S, Huseby ES, Zehn D, King CG. Antigen affinity and antigen dose exert distinct influences on CD4 T-cell differentiation. *Proc Natl Acad Sci U S A* 2014;111:14852–14857.
 56. Barrett JC, Hansoul S, Nicolae DL, Cho JH, Duerr RH, Rioux JD, Brant SR, Silverberg MS, Taylor KD, Barnada MM, Bitton A, Dassopoulos T, Datta LW, Green T, Griffiths AM, Kistner EO, Murtha MT, Regueiro MD, Rotter JI, Schumm LP, Steinhardt AH, Targan SR, Xavier RJ, Libioulle C, Sandor C, Lathrop M, Belaiche J, Dewit O, Gut I, Heath S, Laukens D, Mni M, Rutgeerts P, Van Gossum A, Zelenika D, Franchimont D, Hugot JP, de Vos M, Vermeire S, Louis E, Cardon LR, Anderson CA, Drummond H, Nimmo E, Ahmad T, Prescott NJ, Onnie CM, Fisher SA, Marchini J, Ghori J, Bumpstead S, Gwilliam R, Tremelling M, Deloukas P, Mansfield J, Jewell D, Satsangi J, Mathew CG, Parkes M, Georges M, Daly MJ, Consortium NIG, Consortium B-FI, Control WTC. Genome-wide association defines more than 30 distinct susceptibility loci for Crohn's disease. *Nature Genetics* 2008;40:955–962.
 57. Chiu IM, Heesters BA, Ghasemlou N, Von Hehn CA, Zhao F, Tran J, Wainger B, Strominger A, Muralidharan S, Horswill AR, Wardenburg JB, Hwang SW, Carroll MC, Woolf CJ. Bacteria activate sensory neurons that modulate pain and inflammation. *Nature* 2013;501:52–57.
 58. Ibiza S, Garcia-Cassani B, Ribeiro H, Carvalho T, Almeida L, Marques R, Misic AM, Bartow-McKenney C, Larson DM, Pavan WJ, Eberl G, Grice EA, Veiga-Fernandes H. Glial-cell-derived neuroregulators control type 3 innate lymphoid cells and gut defence. *Nature* 2016;535:440–443.
 59. Zhang Y, Zhang G, Liu Y, Chen R, Zhao D, McAlister V, Mele T, Liu K, Zheng X. GDF15 regulates Malat-1 circular

RNA and inactivates NF κ B signaling leading to immune tolerogenic DCs for preventing alloimmune rejection in heart transplantation. *Front Immunol* 2018;9:2407.

60. Wang W, Qu R, Wang X, Zhang M, Zhang Y, Chen C, Chen X, Qiu C, Li J, Pan X, Li W, Zhao Y. GDF11 antagonizes psoriasis-like skin inflammation via suppression of NF- κ B signaling pathway. *Inflammation* 2019;42:319–330.
61. Wilson AM, Shao Z, Grenier V, Mawambo G, Daudelin JF, Dejda A, Pilon F, Popovic N, Boulet S, Parinot C, Oubaha M, Labrecque N, de Guire V, Laplante M, Lettre G, Sennlaub F, Joyal JS, Meunier M, Sapiaha P. Neuropilin-1 expression in adipose tissue macrophages protects against obesity and metabolic syndrome. *Sci Immunol* 2018;3(21).
62. Frykman PK, Nordenskjöld A, Kawaguchi A, Hui TT, Granstrom AL, Cheng Z, Tang J, Underhill DM, Iliev I, Funari VA, Wester T; HCRG. Characterization of bacterial and fungal microbiome in children with Hirschsprung disease with and without a history of enterocolitis: a multicenter study. *Plos One* 2015;10(4).
63. Saleh MM, Frisbee AL, Leslie JL, Buonomo EL, Cowardin CA, Ma JZ, Simpson ME, Scully KW, Abhyankar MM, Petri WA. Colitis-induced Th17 cells increase the risk for severe subsequent *Clostridium difficile* Infection. *Cell Host & Microbe* 2019;25:756–765.e5.
64. Schirmer M, Smeekens SP, Vlamakis H, Jaeger M, Oosting M, Franzosa EA, Ter Horst R, Jansen T, Jacobs L, Bonder MJ, Kurilshikov A, Fu J, Joosten LAB, Zhernakova A, Huttenhower C, Wijmenga C, Netea MG, Xavier RJ. Linking the human gut microbiome to inflammatory cytokine production capacity. *Cell* 2016;167:1125–1136.e8.
65. Vincent C, Miller MA, Edens TJ, Mehrotra S, Dewar K, Manges AR. Bloom and bust: intestinal microbiota dynamics in response to hospital exposures and *Clostridium difficile* colonization or infection. *Microbiome* 2016;4:12.
66. Mueller NT, Shin H, Pizoni A, Werlang IC, Matte U, Goldani MZ, Goldani HAS, Dominguez-Bello MG. Delivery mode and the transition of pioneering gut-microbiota structure, composition and predicted metabolic function. *Genes (Basel)* 2017;8(12).
67. Pierre JF, Barlow-Anacker AJ, Erickson CS, Heneghan AF, Levenson GE, Dowd SE, Epstein ML, Kudsk KA, Gosain A. Intestinal dysbiosis and bacterial enteroinvasion in a murine model of Hirschsprung's disease. *J Pediatr Surg* 2014;49:1242–1251.
68. Muller PA, Schneeberger M, Matheis F, Wang P, Kerner Z, Ilanges A, Pellegrino K, Del Marmol J, Castro TBR, Furuichi M, Perkins M, Han W, Rao A, Pickard AJ, Cross JR, Honda K, de Araujo I, Mucida D. Microbiota modulate sympathetic neurons via a gut-brain circuit. *Nature* 2020;583:441–446.
69. Struijs MC, Diamond IR, de Silva N, Wales PW. Establishing norms for intestinal length in children. *J Pediatr Surg* 2009;44:933–938.

Received July 14, 2020. Accepted March 9, 2021.

Correspondence

Address correspondence to: Simone Keck, PhD, University Children's Hospital Basel (UKBB), Spitalstrasse 33, 4056 Basel, Switzerland.. e-mail: simone.keck@unibas.ch; fax: +41617041237.

Acknowledgments

The authors thank all the patients and their parents as well as volunteer blood donors for their contribution. They also thank T. Lopes, E. Traunecker, and L. Raeli at the Flow Cytometry Facility of the Department of Biomedicine (Basel) for cell sorting, A. Loynton-Ferrand, K. Schleicher, and O. Biehlmaier at the Imaging Core Facility of the Biocenter (Basel) for assistance in confocal microscopy, D. Calabrese at the Histology Facility of the Department of Biomedicine (Basel) for histological support, N. Ritz and A. Marten at University Children's Hospital (Basel) for Luminex analysis, P. Weigold at Microsynth AG (Balgach) for microbiome analysis, and S. Rogers at MediWrite (Basel) and Fiona Beck for manuscript revision.

Members of the NIG Study Group: Isabella Bielicki, Department of Pediatric Surgery, University Children's Hospital Basel (UKBB) and University of Basel, Basel, Switzerland; Sandra Weih, Department of Pediatric Surgery, University Children's Hospital Basel (UKBB) and University of Basel, Basel, Switzerland; Ueli Moehrlen, Department of Pediatric Surgery, University Children's Hospital Zurich, Zurich, Switzerland; Noëmi Zweifel, Department of Pediatric Surgery, University Children's Hospital Zurich, Zurich, Switzerland; Kai-Uwe Kleitsch, Department of Pediatric Surgery, Children's Hospital of Eastern Switzerland, St Gallen, Switzerland; Carole Gengler, Department of Pathology, University Hospital of Lausanne (CHUV) and University of Lausanne, Lausanne, Switzerland; Kiarasch Mortazawi, Department of Pediatric Surgery, Municipal Hospital, Karlsruhe, Germany; Milan Milosevic, Department of Pediatric Surgery, University Hospital of Bern, Bern, Switzerland; Vera Otten, Department of Pediatric Surgery, Florence Nightingale Hospital, Düsseldorf, Germany; and Lennart Homrighausen, Department of Pediatric Surgery, Florence Nightingale Hospital, Düsseldorf, Germany.

CRedit Authorship Contributions

Simone Keck, PhD (Conceptualization: Lead; Data curation: Lead; Formal analysis: Lead; Funding acquisition: Lead; Investigation: Lead; Methodology: Lead; Supervision: Lead; Validation: Lead; Writing – original draft: Lead; Writing – review & editing: Lead)

Virginie Galati-Fournier (Data curation: Equal; Formal analysis: Equal; Methodology: Equal; Software: Lead; Validation: Equal; Writing – review & editing: Supporting),

Urs Kym (Data curation: Equal; Formal analysis: Equal; Investigation: Equal; Methodology: Equal),

Michèle Moesch (Data curation: Equal; Formal analysis: Equal; Writing – review & editing: Supporting),

Jakob Usemann (Data curation: Equal; Formal analysis: Equal; Writing – review & editing: Equal),

Isabelle Müller (Data curation: Supporting),

Ulrike Subotic (Writing – review & editing: Supporting; patient recruitment and follow up: Equal),

Sasha J. Tharakan (Writing – review & editing: Equal; patient recruitment and follow up: Equal)

Thomas Krebs (Writing – review & editing: Equal; patient recruitment and follow up: Equal)

Eleuthere Stathopoulos (Writing – review & editing: Equal; patient recruitment and follow up: Equal),

Peter Schmittbecher (Writing – review & editing: Equal; patient recruitment and follow up: Equal)

Dietmar Cholewa (Writing – review & editing: Equal; patient recruitment and follow up: Equal)

Philipp Romero (Writing – review & editing: Equal; patient recruitment and follow up: Equal)

Bertram Reingruber (Writing – review & editing: Equal; patient recruitment and follow up: Equal),

Elisabeth Bruder (Resources: Lead; Writing – review & editing: Equal)

Stefan Holland-Cunz, Prof Dr med (Conceptualization: Supporting; Resources: Lead; Validation: Equal; Writing – review & editing: Equal; patient recruitment and follow up: Equal)

Conflicts of interest

The authors disclose no conflicts.

Funding

Supported by the Stay on Track and Research Fund Junior Researcher from the University of Basel, Switzerland (awarded to S.K.; DMS2343).